A Study of the Molecular Mechanics of Wood Cell Walls

by

David Adler
Bachelor of Engineering in Civil Engineering
Cooper Union, 2010

SUBMITTED TO THE DEPARTMENT OF CIVIL AND ENVIRONMENTAL ENGINEERING IN PARTIAL FULFILLMENT OF THE REQUIREMENTS FOR THE DEGREE OF

MASTER OF SCIENCE IN CIVIL AND ENVIRONMENTAL ENGINEERING
AT THE
MASSACHUSETTES INSTITUTE OF TECHNOLOGY

June 2013

Signature of Author: _____
Department of Civil and Environmental Engineering
May 28, 2013

Certified by: _____
Markus J. Buehler
Associate Professor of Civil and Environmental Engineering
Thesis Advisor

Accepted by: _____
Heidi M. Nepf
Chair, Departmental Committee for Graduate Students

A Study of the Molecular Mechanics of Wood Cell Walls

by

David Adler

Submitted to the Department of Civil and Environmental Engineering on May 28, 2013 in Partial Fulfillment of the Requirements for the Degree of Master of Science in Civil Engineering

ABSTRACT

Wood is the original structural material, developed by nature to support tall plants. Every advantageous feature of wood as used in artificial structures is rooted in the plant's evolved capability to withstand the conditions of its survival: specifically wind and gravity loads. Wood resists these load types with remarkable efficiency with performance comparable to structural alloys. Additionally, wood exhibits the ductility and energy dissipation capacity required of structural materials to prevent catastrophic failure. The hierarchical structure of wood allows for a wide range of mechanical properties; through the modulation of various parameters at various length scales, the living tree grows wood with properties fine-tuned to handle the specific loading conditions. This thesis explores why and how this hierarchical structure works, with a focus on the cell wall material of stiff fibrils in a pliant matrix. Here we report a simple coarse-grained model of the fibrils and matrix to provide a bottom-up description of the mechanics. We identify the mechanical behaviors for varying fibril angles, and in addition, for varying fibril lengths, plot force-strain relationships and compare the data with experimental results and theoretical predictions, providing insight into fundamental structure-property relations of wood. While it presents a simple formulation, it can successfully describe several key phenomena, specifically the three regimes of mechanical behavior: elastic, plastic, and high-strain stiffening, as well as the dependence of modulus on the fibril angle, and as such provides a bottom-up mechanistic approach to wood mechanics. Additionally, the intersection of biological inspiration, computer simulation, and three-dimensional printing is discussed highlighting profound implications for future advanced material design. Previous research developed computer simulations of theoretical biomimetic "bone-like" materials, which were then printed as samples for experimentation. A fractured sample is investigated with optical and electron microscopy with emphasis on failure mechanisms and the quality and resolution of the printing process. The observed damage patterns are shown to correlate to the deformation and failure patterns predicted by simulation, an impressive first step towards more advanced biomimetic fabricated materials designed through computer simulation.

Thesis Supervisor: Markus J. Buehler
Associate Professor of Civil and Environmental Engineering

Acknowledgements

I must first thank my parents, who have continued to support me with each step I had taken towards higher education. And my siblings, who, while not always physically near, managed to keep me centered with their perspectives and perceptions.

To Professor Markus J. Buehler, my advisor for this thesis, I owe you many thanks. You are an incredible scientist. Your enthusiasm for the subjects you teach is infectious, and I am glad to have been infected, and glad to have been a member of LAMM.

I would also like to thank Doug Shattuck for our collaboration during the summer of 2012, and our friends at JEOL for excellent microscopy, far beyond the capabilities of our own facilities.

And of course, thank you to all the members of LAMM that I got the chance to work with, you know who you are. You are awesome.

Table of Contents

List of Figures

1. Introduction: Why Wood?

For longer than the collective memory of mankind, wood has been used to build structures, but for even longer than that, nature has been using wood to keep plant life—large and small—standing. Every advantageous feature of wood as used in artificial structures is rooted in the plant's evolved capability to withstand the conditions of its survival: specifically wind and gravity loads. Wood is effective as foundation piles or columns because the tree evolved to support its own massive weight without buckling and it is effective as beams in flexure because the tree evolved to stay firmly to the ground as heavy winds pressure the incredible surface area of its crown. Wood does not simply perform these functions, but, as is common in the biological world, performs them with remarkable efficiency.

In comparison to steel or other engineering alloys, both the density, ρ, and Young's modulus, E, of wood are orders of magnitude lower, however to compare effectiveness, ratios of these two quantities, known as performance indices are the quantities of import. Woods loaded parallel to the grain have a tensile performance index, E/ρ, comparable to that of steel and aluminum, and bending indices, $E^{1/2}/\rho$ for linear and $E^{1/3}/\rho$ for planar, that are greater than those of the metals. This means that in tension, wood has about the same stiffness to weight ratio as steel and aluminum, but in flexure, wood can match the bending stiffness of the alloys at a lower weight, hence a greater efficiency in flexure [1]. These properties are illustrated in **Figure 1**, which plots the density and Young's modulus of engineering materials along with lines of constant performance indices.

Wood also exhibits the ductile behavior that is essential in averting catastrophic failure of structures. This ability to undergo plastic deformation is a critical feature common to both wood and structural alloys, what is fascinating though, is the different mechanisms the two material types employ to achieve this feature. Metals, homogenous to the atomic scale—or at least to the scale of crystal grains—achieve plasticity through the movements of vacancies and dislocations in the atomic matrix. Wood, on the other hand, is hierarchically structured: the properties of bulk wood are derived from the properties and arrangement of the wood fibers (cells), whose properties are, in turn, derived from the properties and arrangement of the wood polymers that make up the cell walls. It is from this lower level of hierarchy, the composition of the cell wall material, that wood derives its plasticity: the wood cells can elongate extensively before fracture through the rearrangement of the hydrogen bonded polymers that make up the cell walls. This mechanism, the focus of this research, is discussed in greater detail in Chapter 2.2.

Aside from its superior performance as a lightweight structural material, use of wood in structures can also be less expensive and more environmentally friendly than using steel. Manufacturing glued laminated timber (glulam) takes two to three times less energy and six to twelve times less fossil fuels than manufacturing a steel member, and if the wood is burned to substitute fossil fuels at the end of its service life, the lifecycle greenhouse emissions are less than for steel [2]. While the clear advantages of wood stem from its origin as a naturally grown material, so too do its disadvantages. Trees of different species produce wood of different qualities, and even within a species, each individual tree in unique, however the most significant

inconsistencies—leading to the greatest uncertainty, with regards to mechanical properties—are within the individual tree. The random elements, such as branching, knotting, and eccentric growth introduce inconsistencies in the strength and modulus of large cuts of wood, forcing a less-than-ideal efficiency in its structural uses, and even the most pure, unknotted log will still have varying stiffness throughout its cross section. In general, wood closer to the center (pith) tend to be softer than wood closer to the bark. When considering a whole log, this variance serves to stabilize the column against buckling, but when standardized sections are cut from the log, the standardized stiffness of the section cannot be guaranteed. Furthermore, the shape and orientation of the cut will have a significant impact on its mechanical properties, and warping characteristics, as illustrated in **Figure 2** [3].

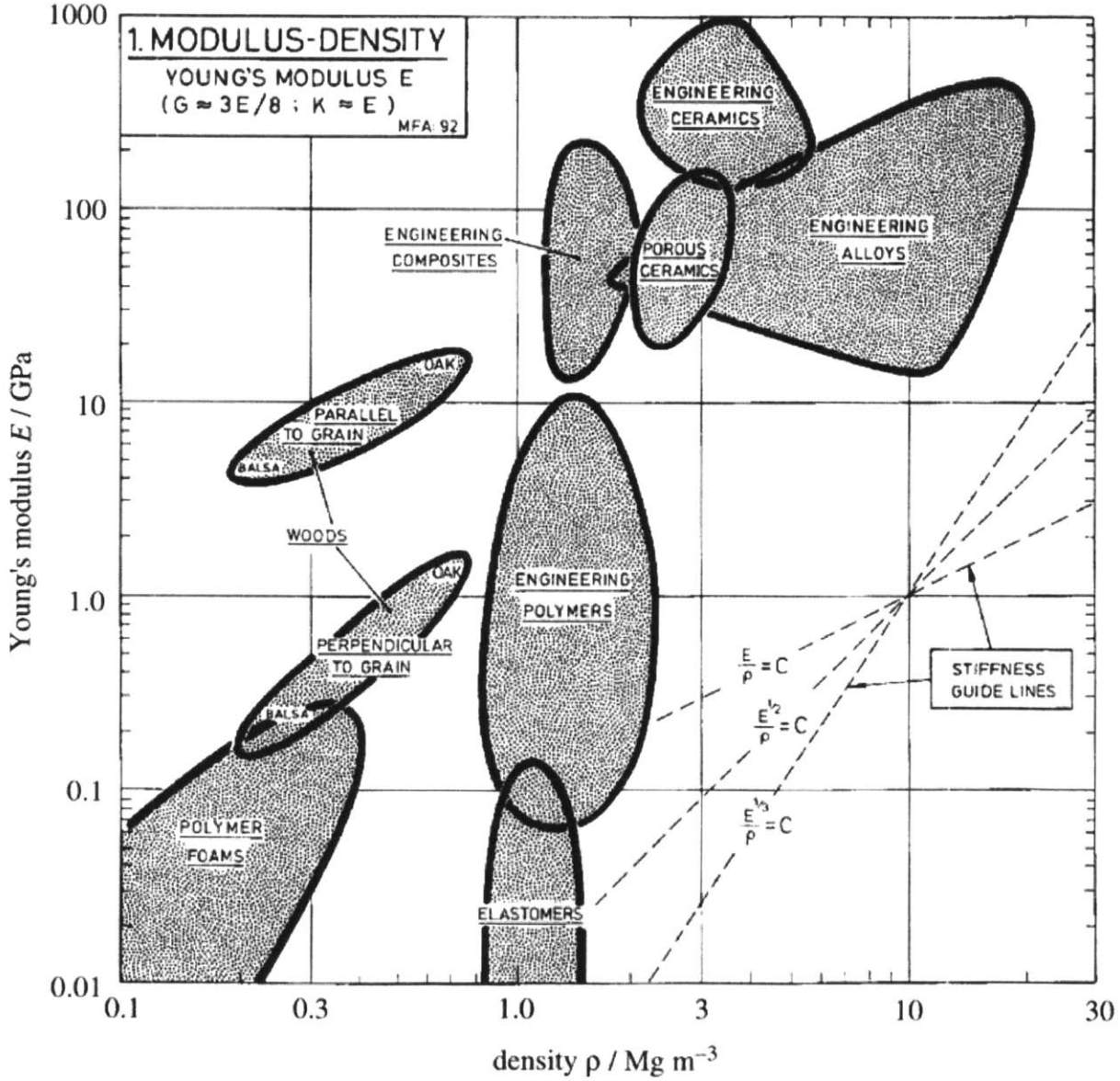

Figure 1: Materials property chart for engineering materials with Young's modulus plotted against density. Reprinted from [1] Copyright 1995 with permission from The Royal Society.

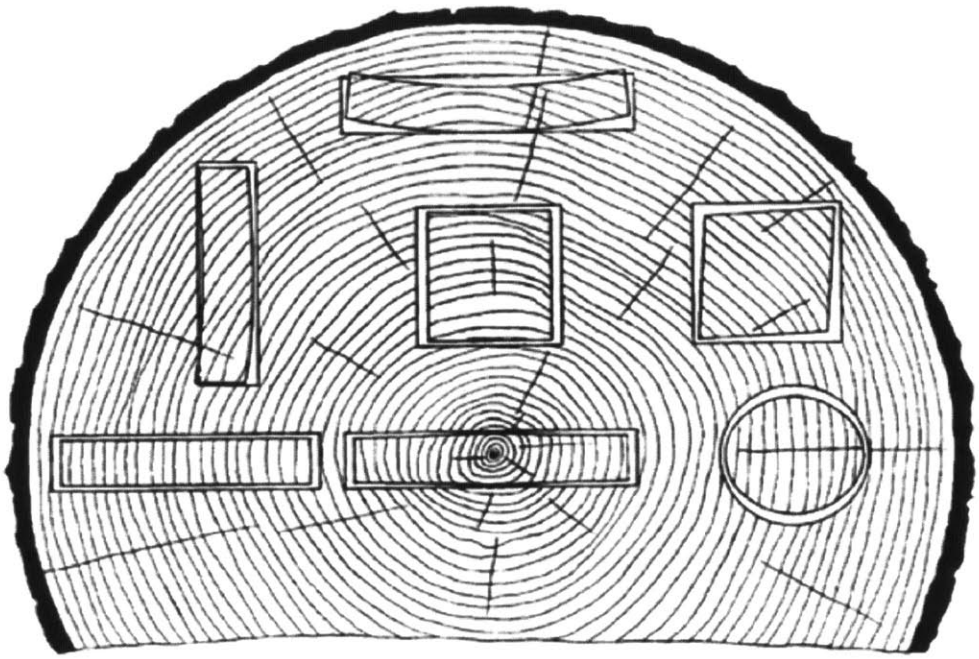

Figure 2: Schematic of warping characteristics of different shapes and location of lumber cut from tree trunks due to variations in stiffness from pith to bark. Reprinted from [3].

Structural lumber and veneers are cut along the grain so that the axes of the cells match the axes of loading. However, since the mechanical properties vary by location in the cross section of the log, the properties of the member differ between cuts. Veneers peeled off from the outer layers of the log may be stiffer than those cut from the center, and similarly, the stiffness of the material might vary significantly over the depth of a beam depending on the section of trunk from which it cut, resulting in warping and irregular deformation and stress distribution.

Engineered structural wood, such as glued laminated timber (glulam), emerge from the effort to make larger, or specifically shaped structural members without introducing the greater mechanical diversity that a larger cut would introduce. Glulam members consist of number of relatively consistent cuts of timber stacked and bonded together to form a large member of precise dimensions—curved and/or straight—with consistent properties. Ultimately though, the properties of the glulam are derived from the properties of the wood, which are limited and imprecise.

A better understanding of how wood functions could lead to breeding or engineering trees to grow wood with specified properties for higher efficiency in structures, or it could inspire artificial materials to mimic the beneficial properties with none of the impurities and inconsistencies. Already, advanced computer modeling can be used to design and test theoretical materials, for example, [4] designed a carbon nanotube based fiber material with polymer crosslinking inspired by wood. Their model was capable of varying parameters and measuring mechanical properties, with the idea of finding optimal parameter values through simulation to guide potential fabrication. Other theoretical materials have drawn inspiration from nature's mineralized materials, such as bone and nacre, focusing on the details of the geometry and the

relative properties of the constituent components [5-7]. And as an early step towards advanced biomimetic materials, some of these geometries were used to template samples fabricated by three dimensional printing and mechanically tested [8]. As we advance our understanding of natural materials, the potential of our computer simulations, and the capabilities of our three dimensional printers, we approach the future of designing and fabricating materials of superior properties chosen specifically for the intended use. The possibilities are nearly limitless, however, the first step is to advance our understanding of the fundamental concepts and mechanisms. The purpose of my research is to open the door to more comprehensive computer models that can provide deeper insight into the mechanisms and advance our understanding of wood and its mechanical properties. I focus on the very basics of one of the fundamental mechanisms. There is much room, however, for expansion, both in terms of advancing models of this mechanism and of developing models to explore other mechanisms.

The impact of such basic understanding is that it provides a firm foundation for a bottom-up description of the material. With the basic model, we elucidate trends in the behavior, dependent on certain parameters at this most basic level that influence the material behavior at each successive hierarchical level. Isolating and identifying such parameters at the fundamental scale will educate the designing of more complex models to test and isolate parameters inherent to their respective scales.

2: How Wood Works

2.1 – The Structure of Wood

Wood, as a highly anisotropic bulk material, is known for its excellent performance under tension and in bending along its strong axis. The mechanical properties, particularly density, Young's modulus, and ultimate strength can take on a wide range of values across the many species. What all species of wood have in common—the reason they are all called "wood"—is their origin as biologically constructed tissue from the stems of plant-life. The excellent properties are the result of the plant's ability to support the massive weights to which it can grow while resisting wind loads and buckling. It is only logical that a material that evolved to withstand such specific loading conditions will be utilized in artificial structures to withstand the same loading conditions. The following sections will discuss the hierarchical features, common to all species of wood and their relation to the properties of bulk wood.

2.1.1 – Cellular Structure

At the macroscopic scale, wood functions as a cellular solid built primarily of parallel hollow tubes, the walls created by the plant cells, typically in the range of 1 mm long and 20 micrometers in diameter [9], "glued" to each other via the compound middle lamella, composed primarily of lignin [10]. Cellular solids, common in nature, tend to be efficient and light-weight and their mechanical behavior is fairly well understood [11]. As long cylinders, rather than the more spherical cells of some other types of plant tissue, the mechanical properties along the cell axis scale directly with the mechanical properties of the cell wall material according to the solid to void ratio in the cross section, which is also a controlling feature of the wood's density, an important determinant in the performance of light-weight structures. The growing plant can vary this ratio, as well as the shape and size in order to adapt to meet some of its biological or mechanical requirements [12]. The geometric anisotropy inherent in the parallel tubular arrangement is responsible for the significant mechanical anisotropy of wood, being far stronger and stiffer parallel to the cells' longitudinal axes [11], and is also a source of its notably lower compressive than tensile strength [12, 13].

2.1.2 – Cell Wall Structure

All cellular materials ultimately derive their mechanical properties from those of the material's solid phase, in the case of wood: the cell wall material. As the next level of hierarchy in the structure of wood, the cell wall material can be considered as a fiber reinforced composite [14]. It is composed of relatively stiff fibrils embedded in a pliant, amorphous, matrix, similar in nature and function to steel rods reinforcing concrete [15-17]. At this level, the properties that the plant can vary are the lengths and thicknesses of the fibrils, the average spacing between them, and the geometric arrangement within the matrix. Generally the fibers are arranged in a helical fashion, encircling the cell, and the pitch angle of the helix, measured with respect to the cell axis is known as the microfibril angle (MFA) [12]. The cell wall is arranged in several

layers, each composed to serve specific functions. **Figure 3** is a schematic diagram of the cell wall structure, noting the primary and secondary cell wall layers and the lamella between cells.

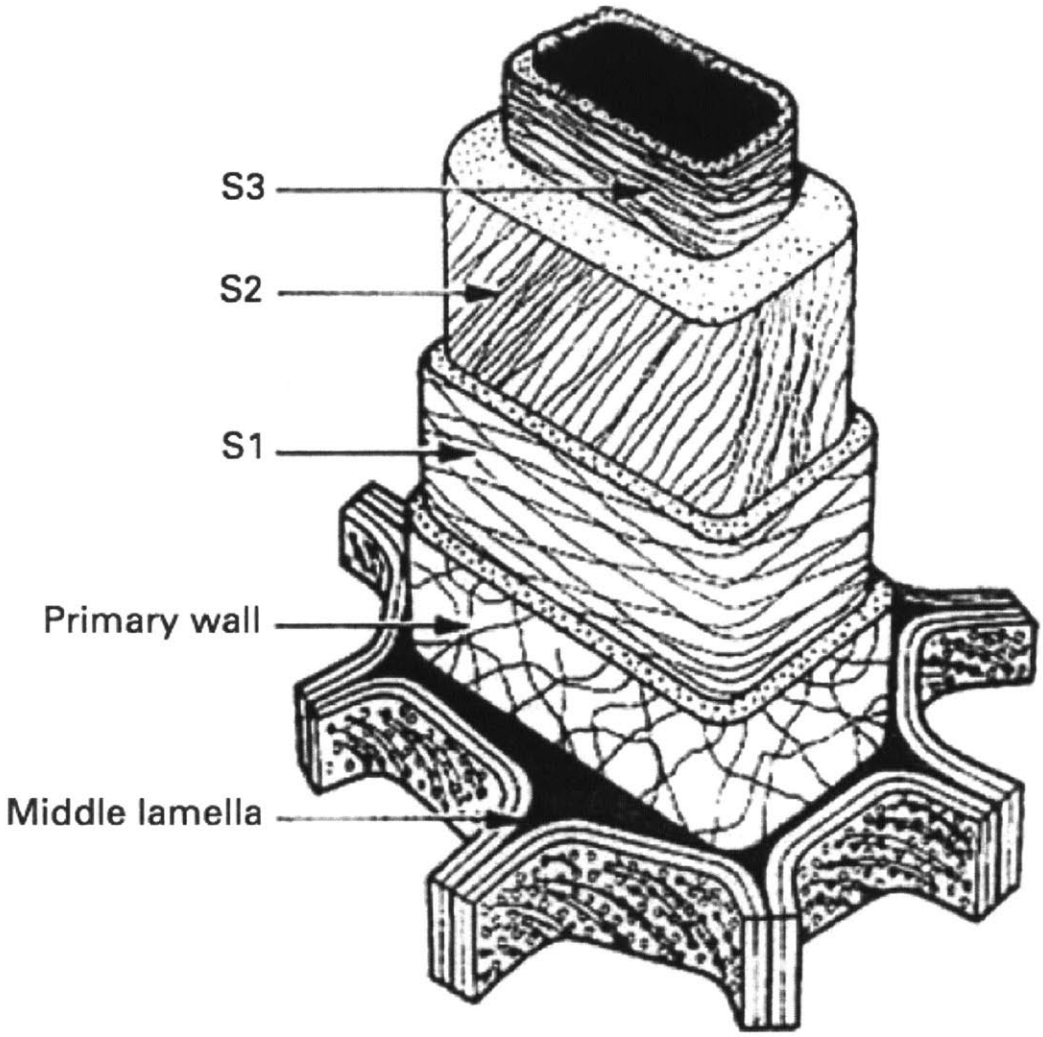

Figure 3: Schematic of the structure of a wood cell, including the middle lamella, primary and secondary cell wall layers. Note the relative coherent fibril orientation of the S2 layer. Reprinted from [18].

The thin outermost layer, the primary cell wall contributes little to the bulk properties, the functions this layer serves involve cell stability: containing the internal cell pressure while allowing and controlling the growth of the cell [17, 19, 20]. The fibers in this layer are arranged nearly perpendicular to the cell axis in order to stabilize the circumference while allowing longitudinal extension [21].Additionally, as it is the outermost layer, it's composition and arrangement are optimized for defense against external fungal and bacterial pathogens [22]. The science regarding the structure, function, and composition of the primary cell wall is extensive; however it is tangent to the focus of this research.

The secondary cell wall is formed by the fully differentiated living cell once it has reached its final shape and size; it is the main source of the strength and stiffness of the cell--and

subsequently of the bulk wood—and continues to provide these qualities even after the cell dies [17]. The secondary cell wall is often subdivided into three layers, S1, S2, and S3, of which it is the middle layer, known as S2, which is the thickest and most prominent contributor of strength and stiffness. In this layer, the fibrils are coherently arranged at a MFA varying from a nearly parallel 5 degrees to a maximum of around 60 degrees [18] depending on the intended function of the cells. In this arrangement, the fibrils in the cell wall behave like springs, allowing for great extensibility by "unwinding" with strain: high MFA wood has a greater unwinding capability and thus can be greatly strained before failure [23]. **Figure 4** shows tensile fracture surfaces for high and low MFA wood, noting the heavy deformation of the high MFA surface due to cell wall fragments spiraling out of the tracheids [24]. Additionally, experimental evidence as well as mathematical models of the cell wall material shows a clear inverse relation between the elastic modulus of the cell to the MFA: the stiffness increases as the angle decreases [23, 25-27], and modulation of the MFA is understood to be the primary technique for the plant to vary its stiffness to adapt to its environment [12] (see Chapter 2.3 for more on this). Whether the fibrils are arranged perpendicular to the middle lamella or tangent to it is a topic of some debate. There is visual evidence supporting the radial arrangement [28-30] and there is visual evidence supporting the lamellar arrangement [31-33], while work by [34] suggests that the arrangement is actually random, shown in **Figure 5**, and that any evidence supporting either a lamellar or radial structure is likely an artifact of the pre-imaging treatment Either way, this feature bears little relevance to the strength and elasticity of the wood cells, and ultimately only plays a part in the details of failure and fracture.

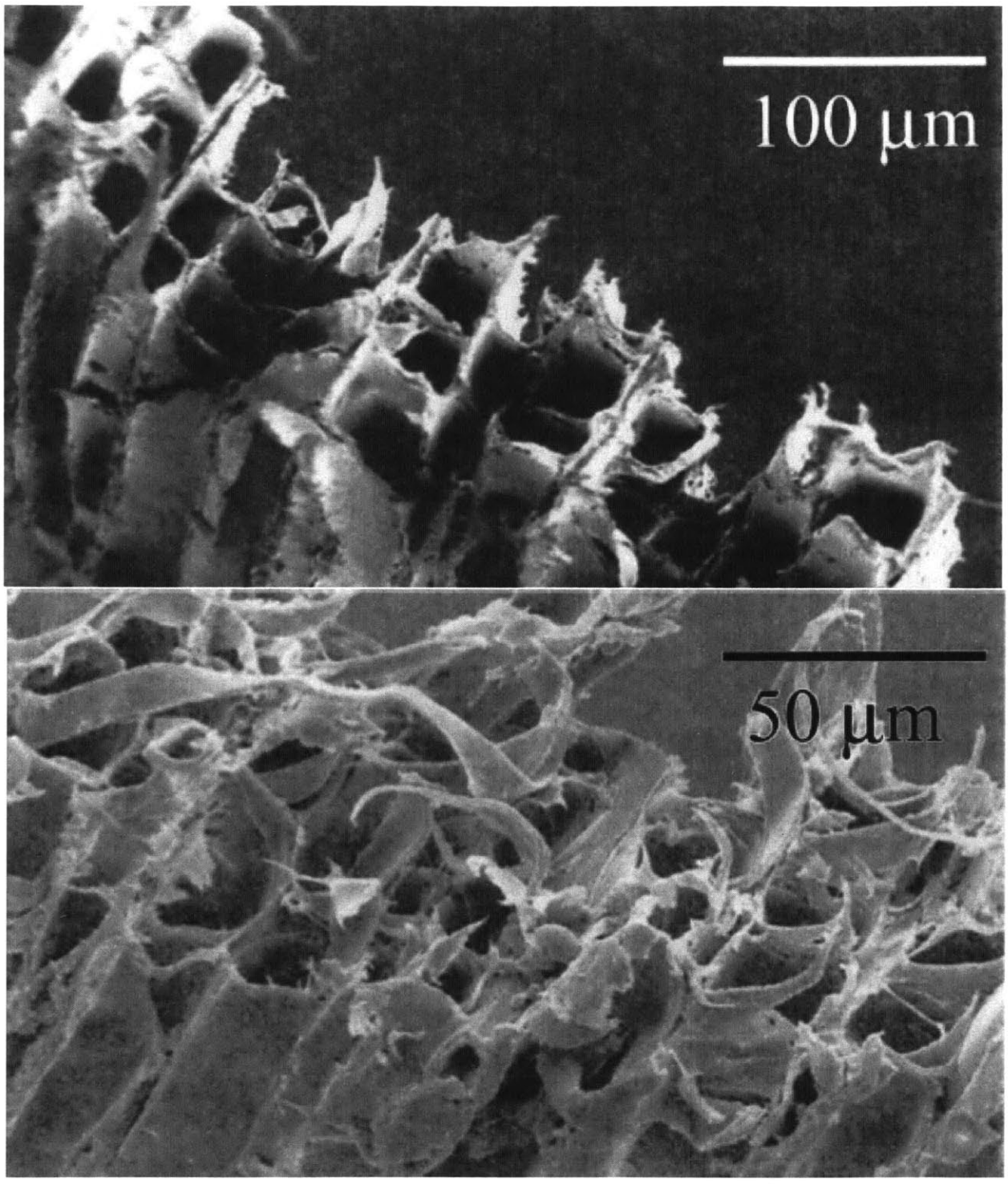

Figure 4: Tensile fracture surfaces of specimens of different MFA. Top panel: MFA of approximately 5° results in mostly smooth surface with little excess damage. Bottom panel: MFA of approximately 50° results in heavily damaged surface as the cellulose helices unwind over a larger strain before fracture. Reprinted from [24] Copyright 2001, with permission from Springer.

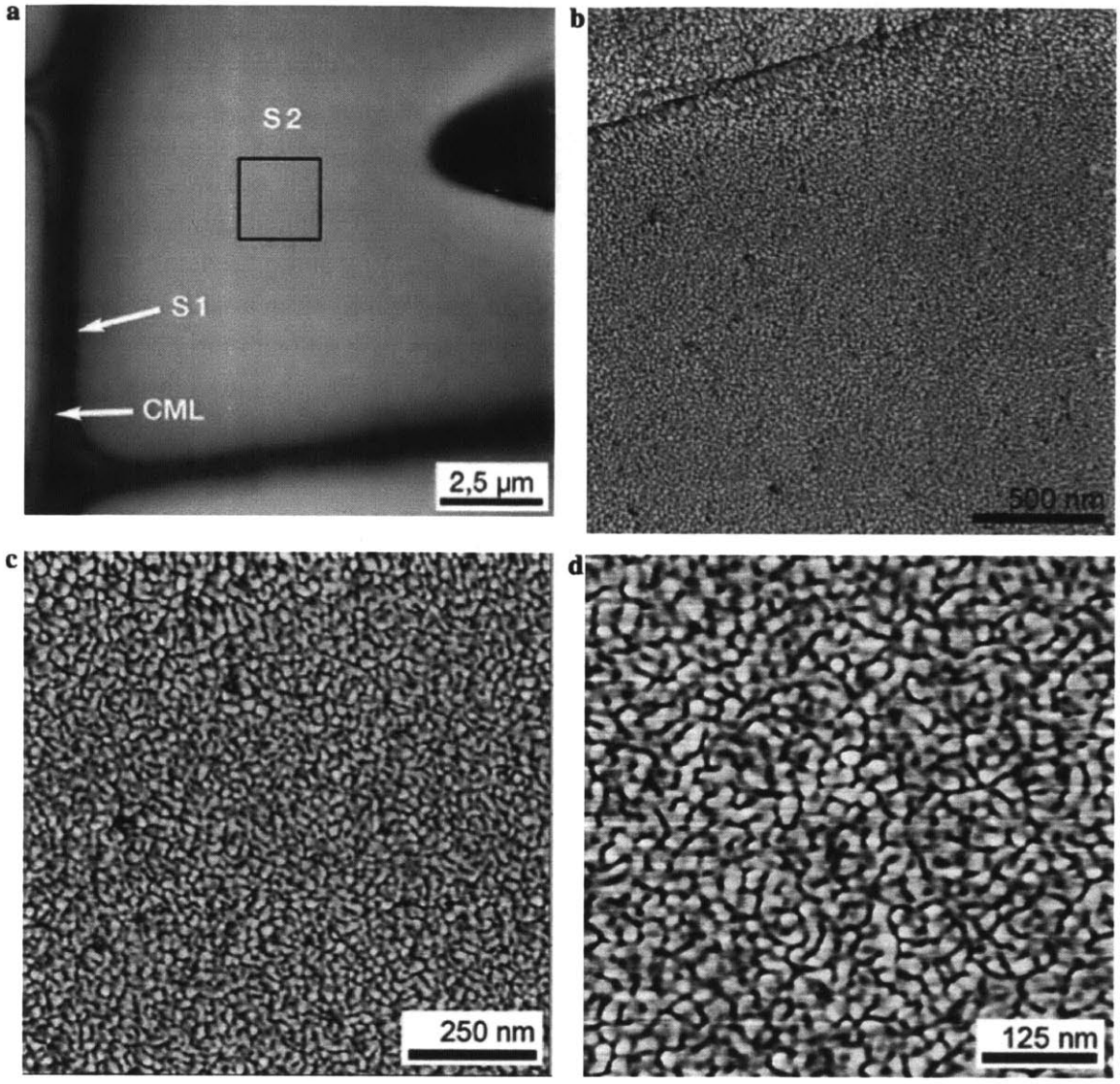

Figure 5: AFM height images of non-dried latewood spruce tracheid. Panel (a) shows the thickness of the S2 layer relative to the S1 and middle lamella. Panels (b), (c), and (d) show successively higher magnifications of the S2 layer. Microfibril aggregates of approximately 15 to 30 nm in thickness are shown with no clear radial or circumferential orientations. Reprinted from [34] Copyright 2006, with permission from Elsevier.

2.2 – Cell Wall Mechanics

The lowest level of the hierarchical structure considers the composition and arrangement of fiber-reinforced composite that is the cell wall material. Visible at high magnification, as seen in panel d of **Figure 5**, the material is a dense network of parallel fibrils embedded in a matrix, similar in some ways to the higher hierarchical structure of parallel cells (also known as fibers) interconnected by the middle lamella. At this level, the behavior of the cell wall material diverges from the previous analogy to reinforced concrete in that the cell wall material remains undamaged and recovers its original stiffness after irreversible deformation. When steel reinforced concrete is over-strained, and the bonding of the concrete to the steel rods is damaged, the material does not recover, whereas within the cell wall the matrix is bonded to the fibers

through hydrogen bonds that are easily reformed once broken. This property is a feature of the chemical structure of the fibers and the matrix.

2.2.1 – Fibrils of Crystalline Cellulose

The basic unit of cellulose, known as cellobiose, is a dimer of glucose monomers, connected by a ß-(1-4) linkage, shown in panel a of **Figure 6** [35]. A single cellulose molecule consists of an un-branched chain of these dimers [36]. When properly aligned, adjacent cellulose chains adhere to each other through a series hydrogen bonds repeating along the length of the chain. Multiple cellulose chains will adhere in this fashion and form hydrogen bonded sheets [35], considered to be the most energetically favorable formation [37] and similarly, the sheets, when properly aligned, will form a network of hydrogen bonds, along the plane of the sheet. These inter-chain and inter-sheet hydrogen bonds stabilize the chains into a firm network known as the I-beta crystal allomorph, shown in **Figure 6**, the most common form of cellulose in plant-life [35, 38, 39].

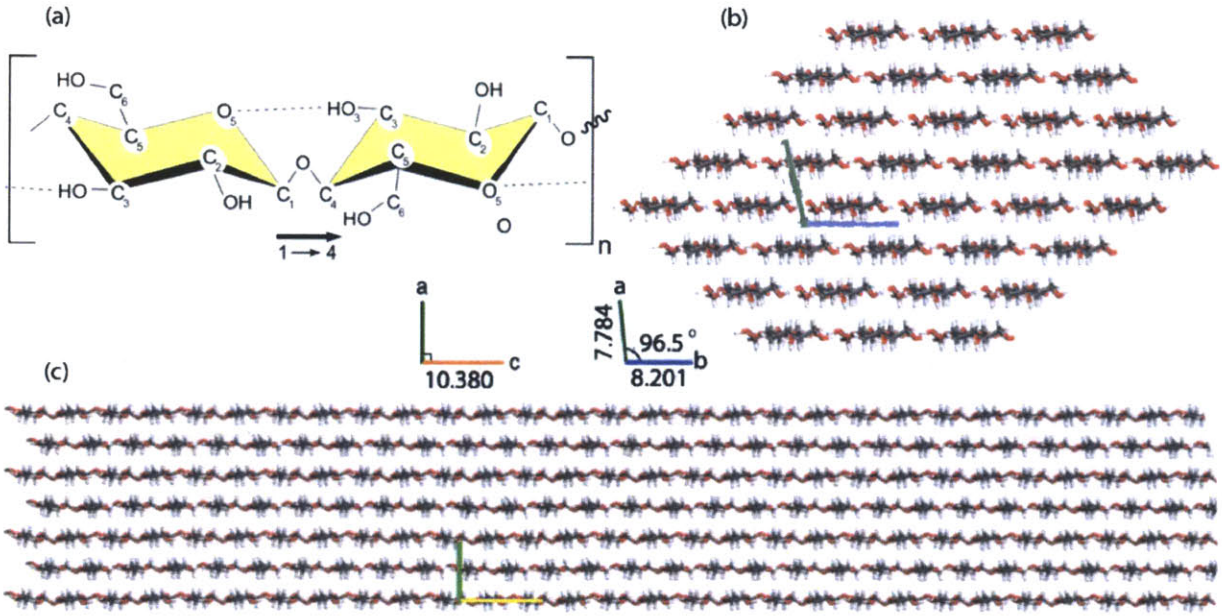

Figure 6: Chemical structure of cellulose. (a) A cellobiose unit of two covalently linked glucose molecules, adapted from [40]. (b) Cross sectional view of a cellulose Iß microfibril, and (c) the side view of the same crystal with unit cell lengths displayed in angstroms, adapted from [41] Copyright 2012, with permission from Wiley.

There is an inherent helical twist to an individual cellulose chain [42], which makes it difficult and hence, unlikely that separate, isolated chains will properly align to form the crystal or even the sheet structure on their own. To overcome this unlikeliness, and actually form the crystal structure, the plant cell builds the microfibril from terminal complexes, synthesizing multiple chains in close proximity, to develop the appropriate hydrogen-bonding pattern as the chains are being constructed [35, 43-47]. While it is difficult to experimentally determine the number of chains per microfibril, it is believed that a 36-chain microfibril, hexagonal in cross section (**Figure 6**) accounts for the estimated 2-4 nm diameter [38, 48-50]. The fibrils that are actually

visually observable through microscopy (as in **Figure 5**) are, in fact aggregates of microfibrils that can range from 10 to 60 nm thick, often referred to as macrofibrils [31, 51, 52]. The reason these macrofibrils are considered as microfibril aggregates instead of as simply larger cellulose crystals is due to the degradation of the crystal structure at the edges of the microfibril as well as a natural twisting that has been determined through microscopy [39, 53, 54] and molecular dynamics simulations [35, 55, 56]—likely a result of the natural twist of the individual chain [57]—that only allows coherent alignment of hydrogen bonds over relatively short segments rather than the entirety of the molecule's length.

2.2.2 – Matrix of Lignin and Hemicellulose

While the structure of the cellulose microfibrils is essentially consistent in all species of wood, the composition of the matrix in which they are embedded is a property that varies between types and species of wood. There is extensive literature on the subject of wood polymers, and their arrangements and behaviors [58, 59]. This introduction will not focus on the specific structures, but rather on the general behavior and contribution of hemicellulose and lignin in the secondary cell wall.

The term hemicellulose was originally used to identify plant polysaccharides extractable via aqueous alkaline solution, thought to be precursors to cellulose. Now known to be incorrect, the term is still used to refer to non-starch polysaccharides found, associated with cellulose, in higher plant cell walls [58]. While there are many different hemicelluloses found in nature, they all share structural-chemical similarities with cellulose, and as such, are able to form hydrogen bonds to cellulose chains the same way that cellulose chains bind to each other. They are even capable of repeated bonds over significant lengths, which are the source of their behavioral analogy to the cement in reinforced concrete: they form a matrix that binds the cellulose fibrils together. The matrix, fundamentally, is composed of hydrogen-bonded polymers, and thus the presence of moisture causes the matrix to swell (which can produce interesting behavior—see Chapter 2.3) as the water molecules fill in the space between polymers and stick to hydrogen bond sites, effectively softening the matrix. Enough moisture can effectively soften the connections of the matrix to the fibrils, which allows large amounts of plastic deformation to be achieved without fracturing the wood (somewhat similar to cold-working of steel).

Where hemicellulose acts as the cement in the composite, lignin would act as the rock and sand filler [10]. Lignin is a cross-linked aromatic polymer [25] which varies from a more branched structure in the middle lamella and primary cell wall to the normal, less branched structure in the secondary cell wall [59]. In the secondary cell wall, the high lignin content in the inter-fibril matrix is understood to be responsible for giving it rigidity while the hemicelluloses—in some cases, capable of covalently bonding to lignin [25]—mediate the interactions with the cellulose fibrils [13, 60, 61].

In many ways the analogy of cell wall material to steel reinforced concrete is appropriate, however where reinforced concrete becomes ineffective once the concrete de-bonds from the steel, in the cell wall, the matrix will re-form the hydrogen bonds to the fibril and recover its original stiffness [62]. This deviation from the analogy is the source of the elastic-plastic

behavior in bulk wood: a behavior similar to structural metals but by a completely different mechanism at completely different scale.

2.3 – Growth and Adaptability of Wood

Functional forms, a theme common throughout the living world, are particularly prevalent in plant stems. In general the functions plant stems involve mechanical stability, transport and storage of water and nutrients, self-repair and adaptive growth, and thermal insulation [13]. Wood is the wonder-material that nature formed to serve all of these functions.

The growth of wood begins with the formation of the primary cell wall, the outermost boundary of each cell. The fibrils in this layer are arranged nearly perpendicular to the cell axis to allow for non-damaging plastic deformation as the cell grows [22]. Once the cell has reached its full size, it starts building the thick secondary layer, synthesizing microfibrils and aligning them at a uniform angle [17]. A plant will build itself with the ideal properties to handle the both the external, environmentally imposed loads and the internal self-weight as it grows.

2.3.1 – Vertical Stability

Tree trunks and branches thicken over the course of their growth by apposition of cells at the exterior. In environments with clear seasonal cycles, a tree will develop visible growth rings as it cycles between building thin-walled earlywood, and thick-walled latewood, shown in **Figure 7**. As the cells die at the end of their differentiation [63], the history of the tree is essentially stored within these growth rings. Shown in **Figure 8**, a clear trend of decreasing MFA (and thus, increasing stiffness) has been measured in the cells pith to bark, implying that the trunk of the young tree was soft and flexible, and then stiffened as it grew. From a mechanical loading standpoint, this trend makes strategic sense: a young tree with a thin trunk does not have a large vertical load to withstand, and is optimized to escape lateral wind loads by bending significantly, while the older tree has a thicker trunk to resist buckling due to the much larger vertical loading and with that increased diameter, it can no longer bend out of the way of lateral wind loads and develops stiff wood to be able to withstand them [12, 64]. This observed MFA gradient is one feature of the growing tree's adaptability, but it is simply an indicator of a larger scale transition in the wood structure. The cells in adult wood (from the outer growth rings), known as normal wood, tend to be mostly rectangular in shape, with a very low MFA of 10 degrees or less, while the cells from the tree's core, known as compression wood, tend to be round with a high MFA in the vicinity of 45 degrees and a notably different chemical composition [63]. Furthermore, the growing tree is known to develop pre-stresses in the cells, inducing compression in compression wood and tension in normal wood [65, 66], to add to the vertical stability of the trunk. A similar technique is used to stabilize tall structures against wind and seismic loading: known as the outrigger system, rigid members extend laterally out of the central building core and attach to tension members tied to the ground.

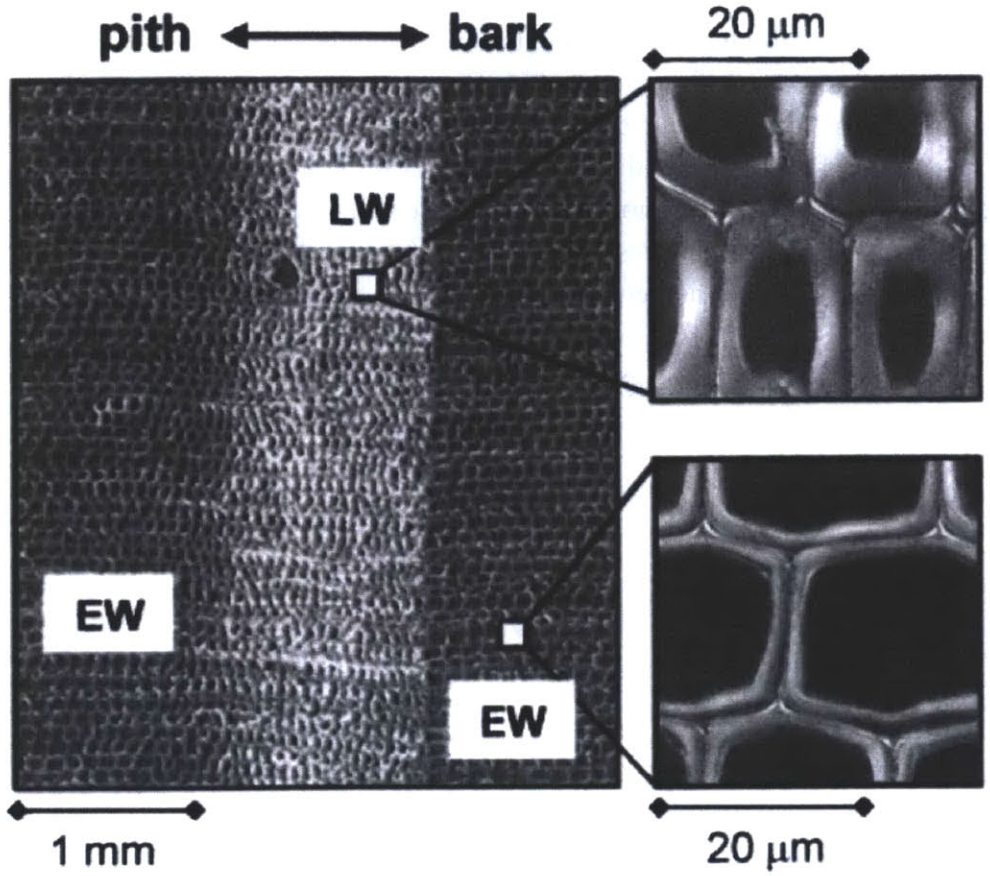

Figure 7: Microscopic image of a growth ring of *Picea abies*. Note the thick walled latewood (LW) cells and the thin walled earlywood (EW) cells. Reprinted from [64] Copyright 1999 with permission from Elsevier.

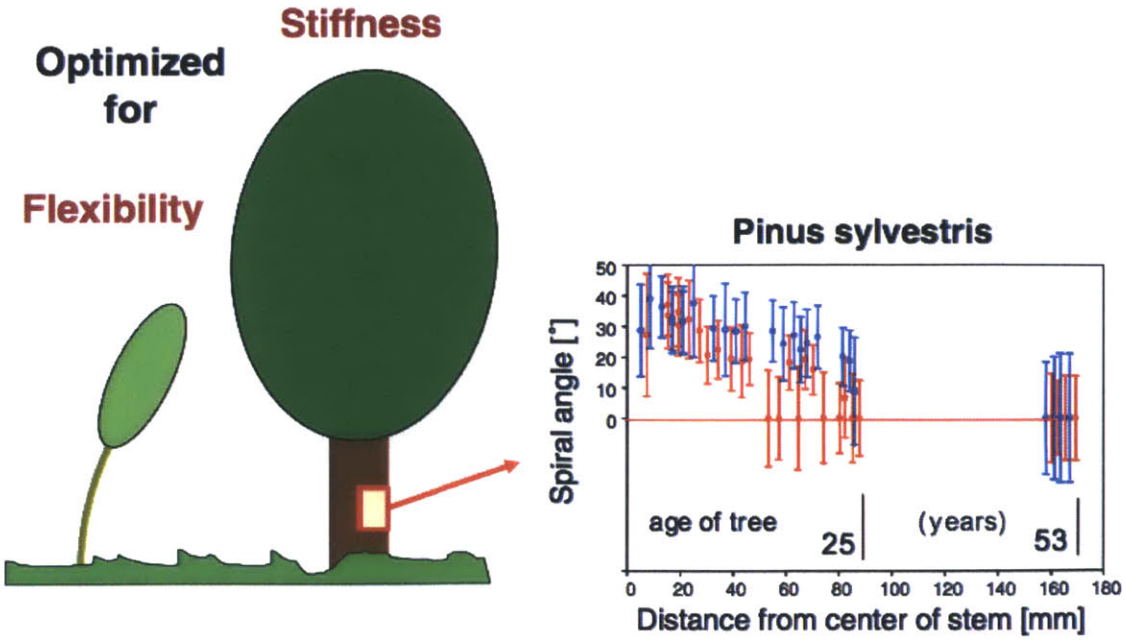

Figure 8: MFA variation from pith to bark highlights the flexibility of the young tree and the stiffness of the adult tree. Reprinted from [12] Copyright 2007 with permission from Elsevier.

Self-supporting trees, as described above, grow significantly stiffer wood as they age in order to cope with the changing structural requirements, however, other plant types may display alternate stiffness-age trends to cope with various other stability mechanisms. **Figure 9** charts the stiffness of three growth forms over the course of maturation, exemplifying the wide range of wood properties that nature is capable of producing to support life. The semi-self-supporting plants are characterized by a high stiffness modulus that is essentially constant throughout its ontogenesis as they rely, throughout their lives, on the supporting structures to cope with many of the loading conditions, and simply must remain stiff enough to continue this reliance. The lianas show the opposite trend of the self-supporting trees: at the younger stages, high stiffness allows them to span the gaps to reach new supports, however once established, greater flexibility is advantageous to shed forces associated with the bending and swaying of the supporting structure [13].

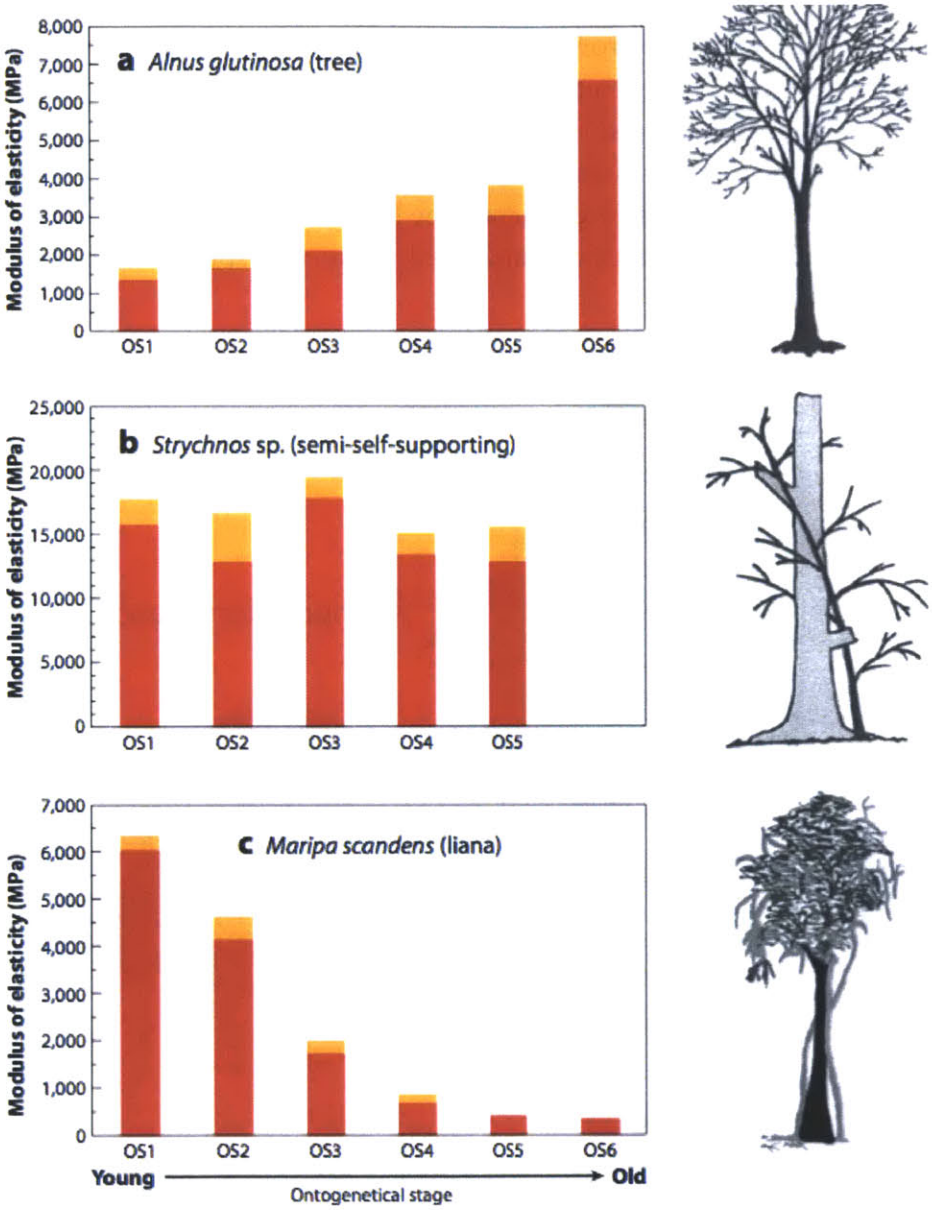

Figure 9: Variations of Young's modulus with age of three growth forms. Reprinted from [13] Copyright 2011 with permission from Annual Reviews.

2.3.2 – Pre-stress

In addition to the outrigger style pre-stressing scheme discussed in the previous section on vertical stability, trees and plants will, by the same mechanism, develop internal stresses to handle unbalanced loads. A tree growing diagonally out of a sloped surface develops massive moment on the lower section of the trunk as the weight of the tree increases. To deal with this imbalance, and alter the growth direction, the tree will grow cells that generates internal tensile stress, known as tension or normal wood, on one side and compressive stress generating cells, known as compression wood, on the other side, generating an internal moment to offset the gravity induced moment. Shown in **Figure 10**, tension wood cells tend to be more rectangular in

cross section and have a low MFA while compression wood cells tend to be more rounded with a high MFA [65]. This phenomenon of reactive growth is also excellently exemplified in branches: as long and heavy cantilevers, they can develop massive bending stresses near the support and grow stiff, low MFA tension wood at the top and flexible, high MFA compression wood at the bottom to maintain orientation as the tree grows and the branch thickens. **Figure 11** details this MFA distribution in branches. A measure of how efficiently the tree grows the ideal wood is that the stress and strain distribution in such junctures was measured, in Norway spruce, to essentially homogenous [13, 67].

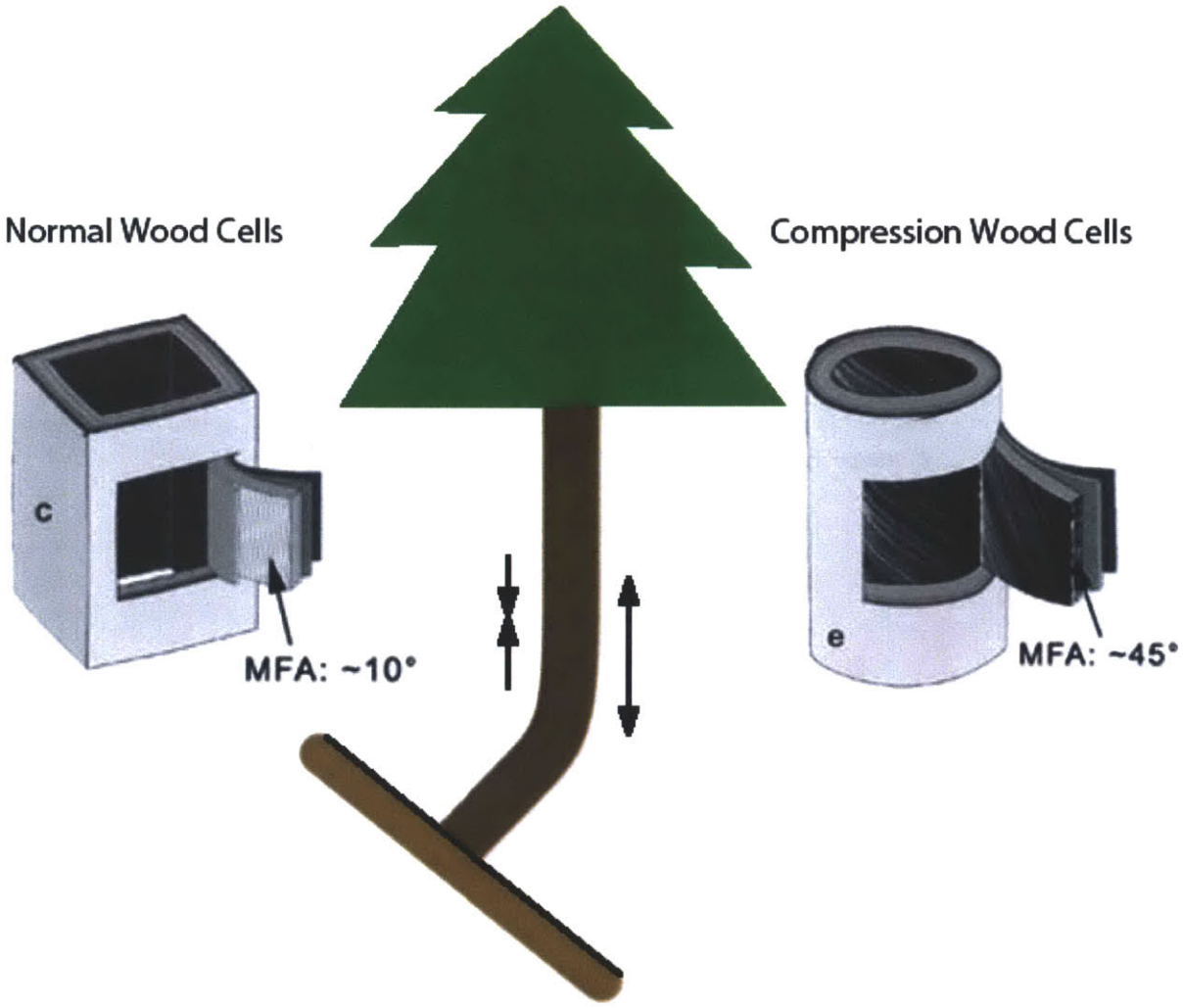

Figure 10: Rectangular tension cells and round compression cells re-orient a tree growing out of a sloped surface. The tension cells with low MFA and fixed torsion (due to rectangular shape) induce tension to pull the tree upright, while the compression cells of high MFA and free torsion induce compression to push the tree upright. Cell schematics reprinted from [63] Copyright 2007, with permission from Springer.

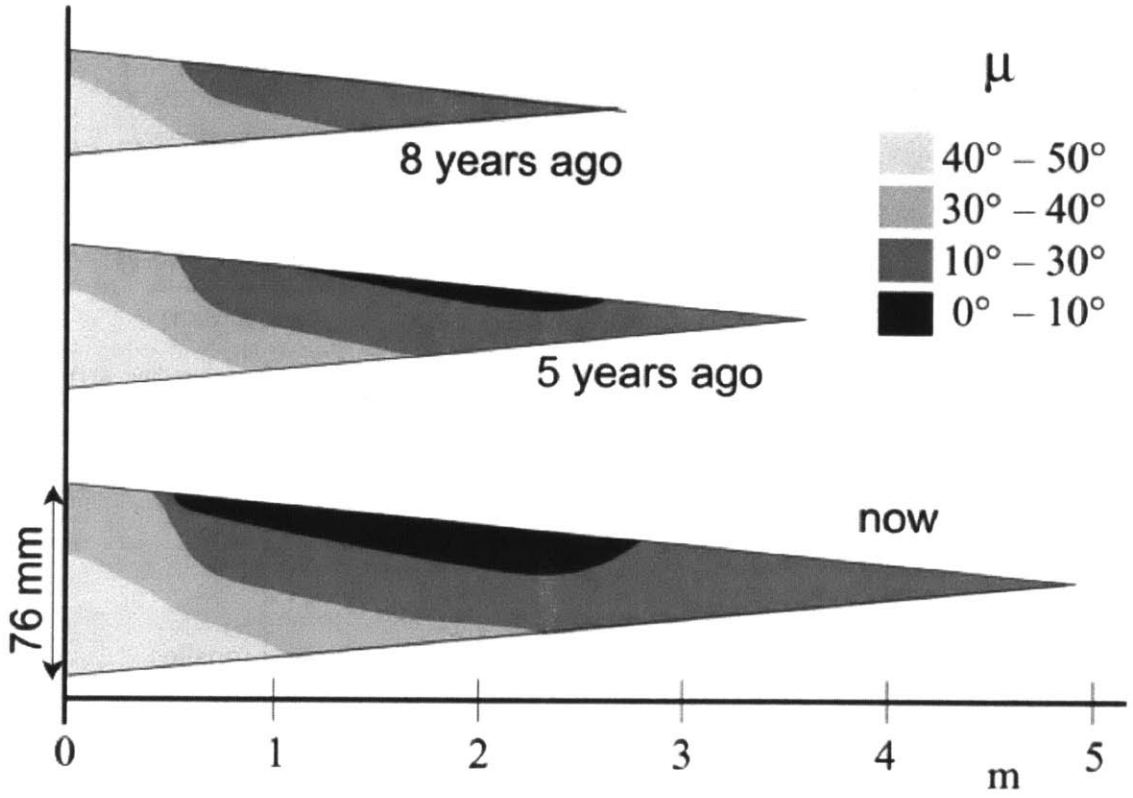

Figure 11: Microfibril angle variation within a branch of spruce. Reprinted from [68] Copyright 2001, with permission from Springer.

The mechanism behind the pre-stress generation involves the swelling of the cell wall and is dependent on the MFA and geometric constraints. Experimental evidence shows the natural elongation of unconstrained compression wood cells and the contraction of unconstrained normal wood cells during swelling [63], which, when constrained would induce internal compression and tension respectively. Mathematical models have been developed to explain this behavior; **Figure 12** is a schematic representation of the mechanism under the simplifying assumption of inextensible cellulose fibrils, and **Figure 13** shows a graphical representation of the mathematic expressions developed by Fratzl, Elbaum and Burgert for various ratios of fibril to matrix stiffnesses [63, 65]. An interesting observation from these models is that the predicted optimal MFA for pre-tensioning (approximately 25 degrees) is very close to the observed MFA in the normal wood of spruce branches and stems subjected to wind loads [69]. Additionally, the model predicts that cells under torsional constraint can generate internal tension, depending on the MFA, whereas if any torsion is allowed, compressive stress will be generated. The rectangular cells and high lignin content of the middle lamella of normal wood effectively prevent the cells from twisting, enacting this torsional constraint and along with the low MFA tension is generated, while in contrast, the low lignin middle lamella and round cells of compression wood effectively leave the cells unconstrained in torsion [63].

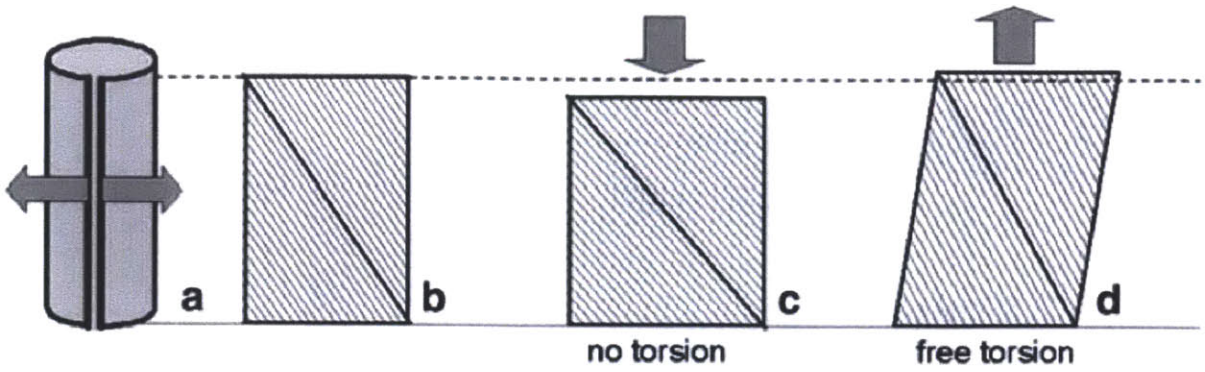

Figure 12: Schematic of inextensible fibril model for cell wall. When the total area is increased due to swelling, preventing torsion causes the cell to contract, while allowing it causes the cell to extend, respectively inducing internal tension or compression. The black line is of constant length, representing the inextensibility of the fibrils in this model. Reprinted from [63] Copyright 2007, with permission from Springer.

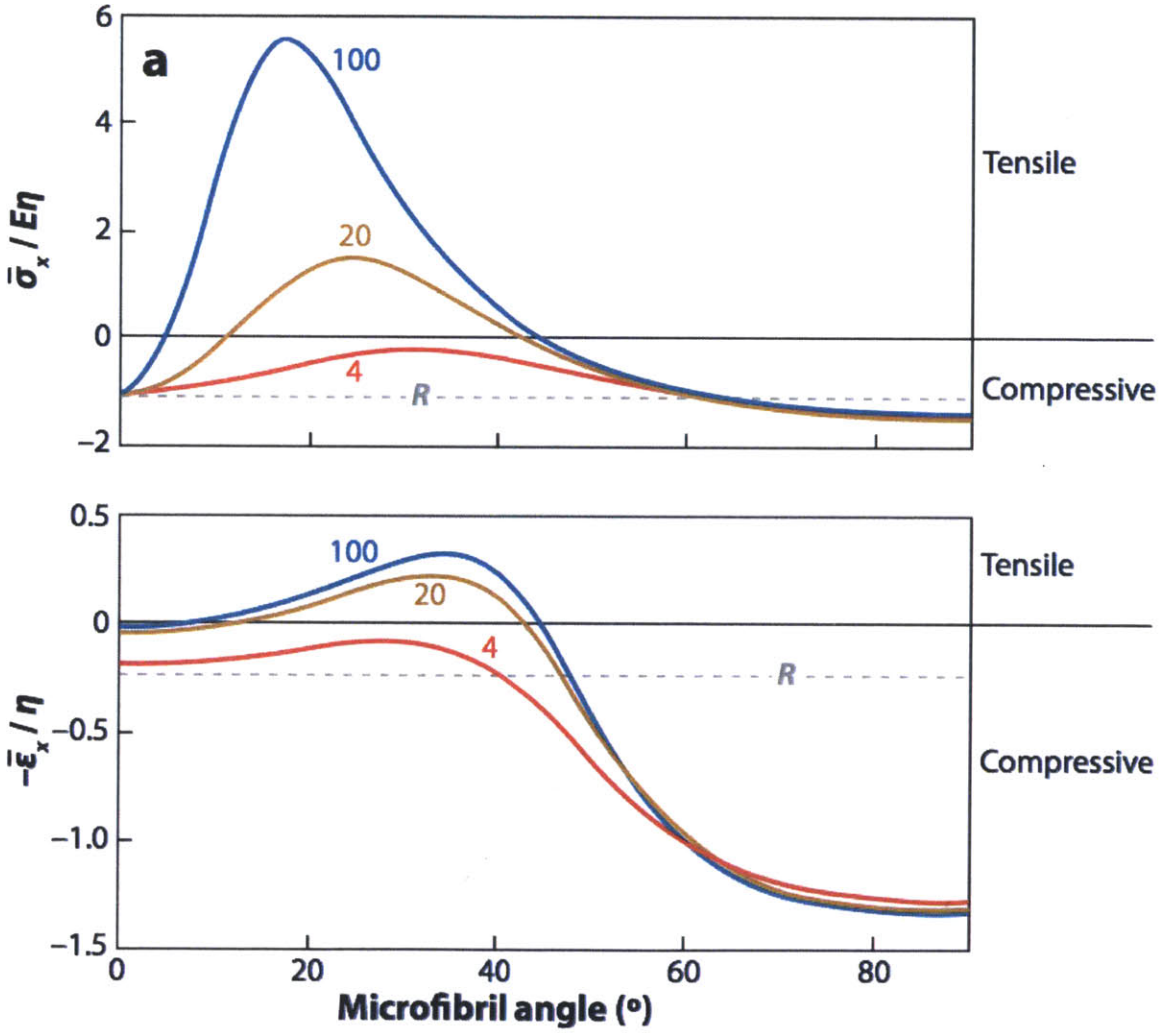

Figure 13: Mechanical effects due to swelling of the cell wall under constrained torsion as a function of MFA for three ratios of fibril to matrix stiffness. (top) Stress generated when the cell is not allowed to change length, and (bottom) strain generated with no applied stress. The lines denoted by "R" represent the stress or strain generated with a random distribution of MFA and a stiffness ratio of 20 (close to the actual ratio). Both plots are normalized by isotropic volume strain due to swelling, η. Reprinted from [69] Copyright 2010, with permission from Annual Reviews.

2.4 – Balsa Wood

Characterized by its exceptionally low density, species *Ochroma pyraåidale,* known commonly as balsa has been used for centuries in lightweight applications. The balsa tree is a fast growing pioneer plant, growing mostly in Central and South America; it can grow up to 5 meters a year to a maximum height of around 30 meters, with a density range from 40 to 320 kg/m^3 depending on habitat or growth speed [70, 71]. Around 500 A.D., the Peruvians used the raw tree to build rafts to navigate the pacific, and it is still used today in flotation devices. It has been used to build lightweight gliders and the U.S. military used it as a skin for the World War II Mosquito. More recently it is used as a core material in sandwich composites for wind turbine rotors.

Sandwich composites are used in a variety of applications, including wind turbine rotors and ship hulls, due to their ability to carry transverse loads, their superior bending stiffness, and low weight. Typically they consist of surface skins surrounding lightweight cores. Because of its low density and excellent shear and bending properties, balsa performs this role excellently. With respect to other core materials, such as PVC foam, balsa is shown to perform equally or better in impact tests [72]. Additionally, due to its ordered and oriented structure, it can be used more efficiently than unordered foams for the very directional loading conditions in wind turbine rotors. Artificially manufactured fiber-reinforced honeycomb composites, mimicking balsa's structure, while controlling the properties and geometry, may be designed to perform this role even more efficiently with further study.

2.4.1 – Cellular Structure

The cellular structure of balsa is fairly regular and well documented. As seen in the micrographs in **Figure 14** courtesy of JEOL, and the schematic diagrams from Easterling, Harrysson and Gibson, in **Figure 15** balsa consists mostly (by volume) of long hexagonal prism cells parallel to the tree's longitudinal axis with the occasional larger sap channel, also parallel and penetrating the entire structure. Blocks of these cells are separated by radial rays that consist of smaller, differently shaped cells, giving the material its three-directional isotropy: axial, radial, and tangential. Growth rings can be discerned at the macroscopic scale, however due to the lack of major seasonal variation, the differences between late and early wood are minute, and hardly discernable in the microstructure.[71, 73]

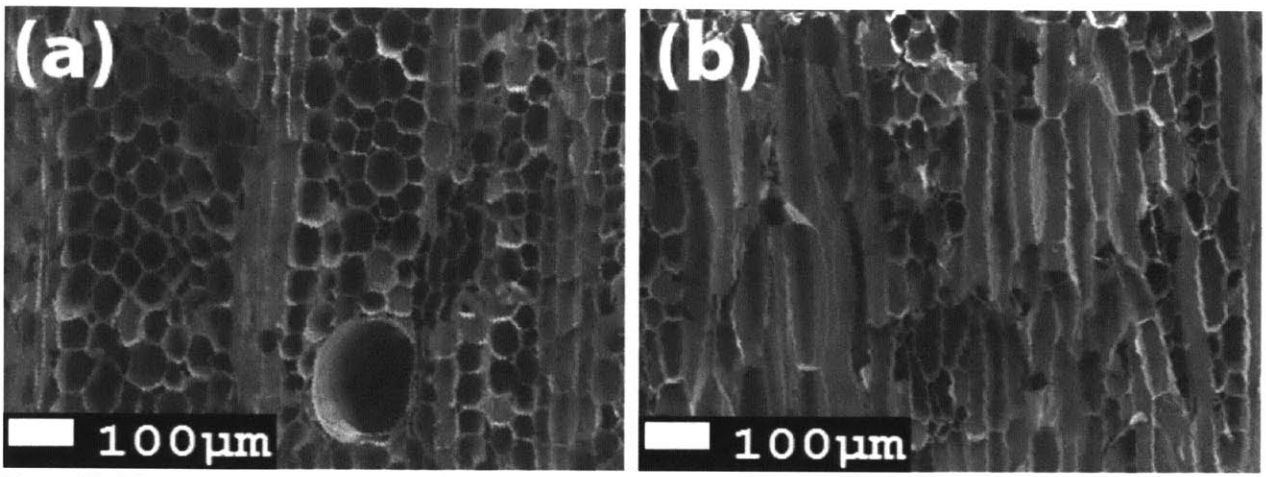

Figure 14: Micrographs of balsa wood. (a) View along longitudinal axis: top-down view of honeycomb structure separated by rays. The large empty tube is a sap channel. (b) Side view: long cells are of the honeycomb hexagonal structure, separated by the smaller cells of the rays. Micrographs courtesy of JEOL USA.

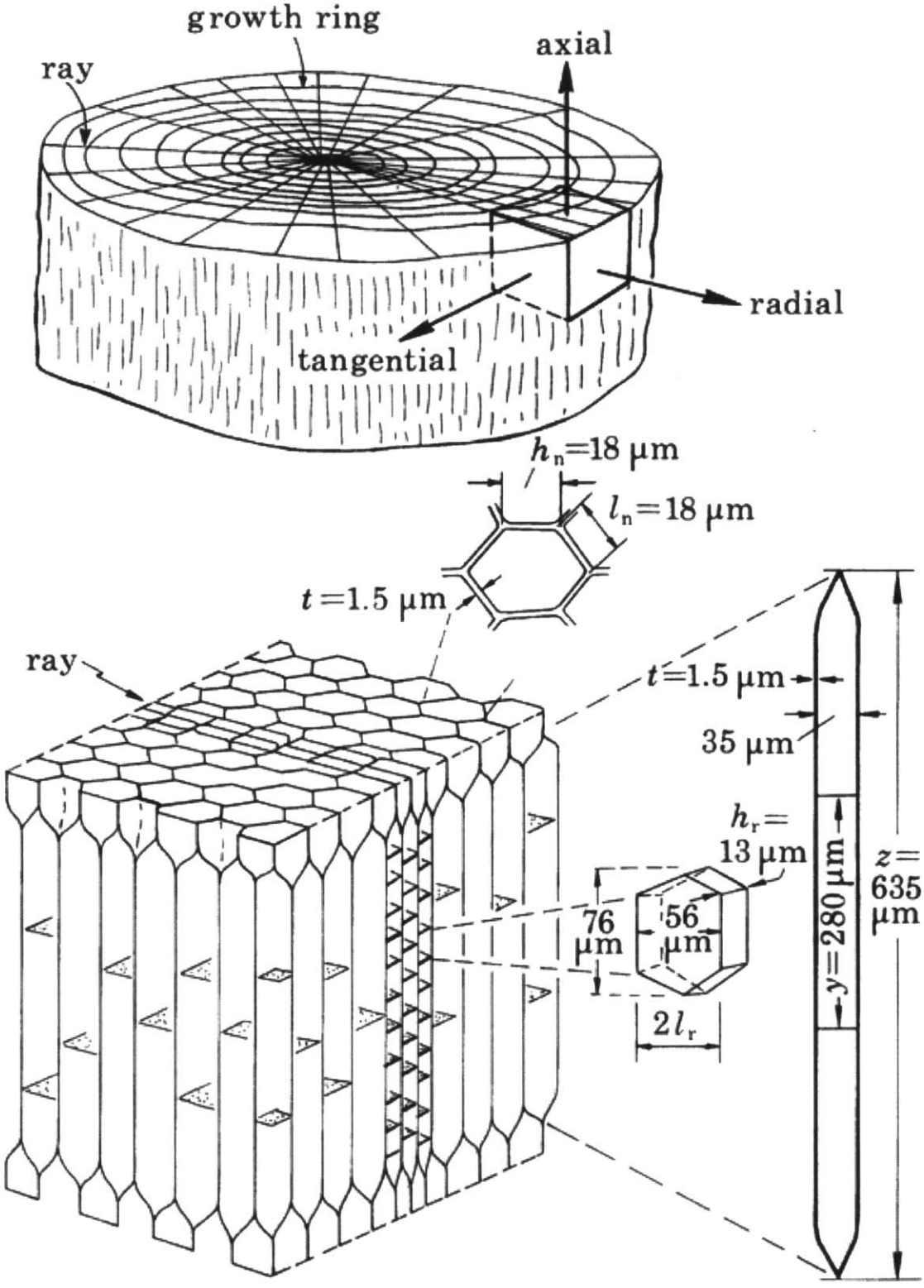

Figure 15: Schematic diagram of general structure of balsa wood, including approximate dimensions. Reprinted from [71] Copyright 1982, with permission from The Royal Society.

2.4.2 – Deformation Mechanics and Energy Dissipation

A typical stress-strain plot for compression of balsa along the three principal directions is shown in **Figure 16**. In the two transverse directions, radial and tangential, compressive deformation is characterized by the bending of the hexagonal cell walls. In the tangential direction, this compressive failure is essentially uniformly distributed however radial compression, due to the orientation of the ray cells, collapse begins at either end of the sample and propagate inward; the direction of compression with respect to the orientation of the rays is illustrated in **Figure 17** In both these directions, the collapse continues up to densification, characterized a drastic increase in stiffness as the cellular collapses entirely and the material ceases to deform through the bending of cell walls but by compressing the densified material directly. Under axial compression, the cell walls do not bend, but undergo direct compression, resulting in the far greater stiffness, as plotted in **Figure 16** up to the point where the pyramidal cell caps collapse, denoted by cutting plane A-A in panel c of **Figure 17**. After this initial collapse, or even instead of, in some cases, the cells will continue to deform either by cell wall buckling, or formation of kink bands, hovering around some plateau stress.

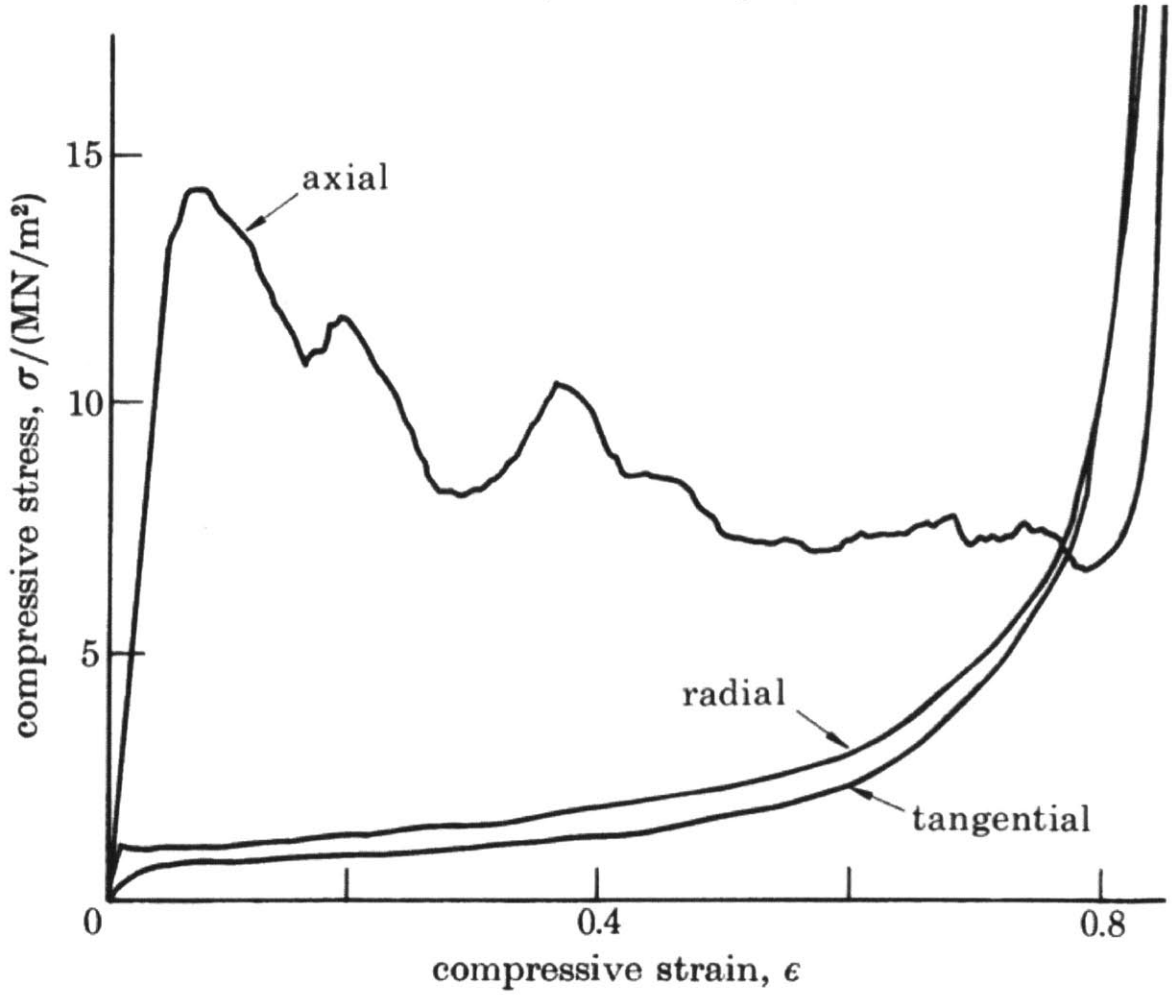

Figure 16: Compressive response of medium weight balsa wood in three principal directions: axial, radial, and tangential. Reprinted from [71] Copyright 1982, with permission from The Royal Society.

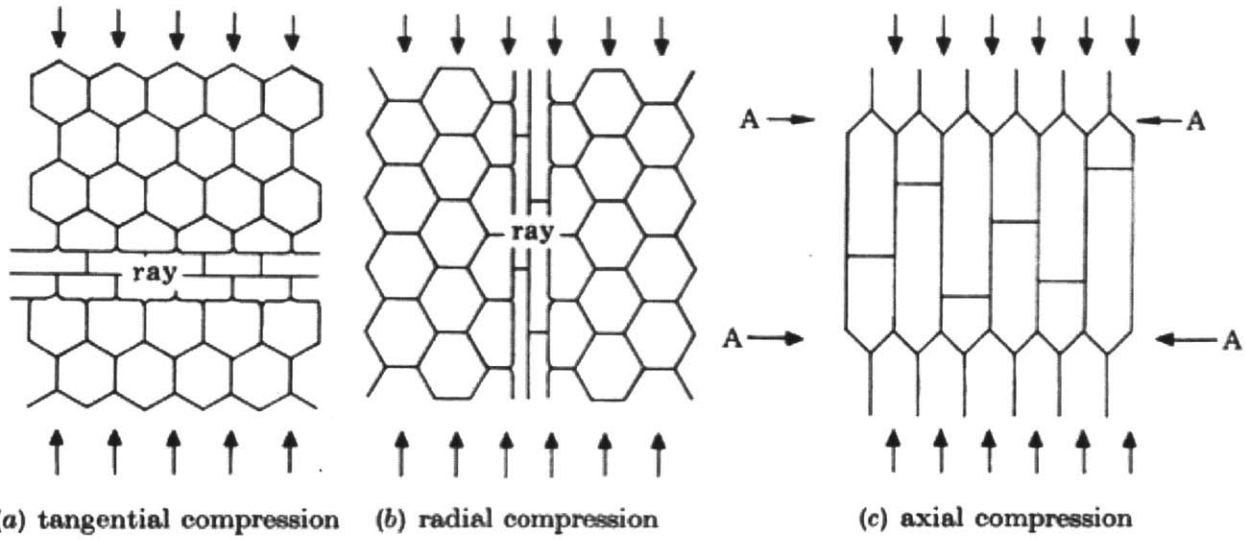

Figure 17: Schematics of three principal loading directions. (a) Tangential compression, perpendicular to rays, allows for uniform cell collapse, as opposed to (b) radial compression, where the stiffness variation due to the ray cells prevents that uniform collapse. (c) Axial compression directly compresses the cell walls without bending; collapse begins with failure of the cell caps, denoted by the A-A planes. Reprinted from [71] Copyright 1982, with permission from The Royal Society.

The choice between these two deformation modes, illustrated in **Figure 18** is primarily determined by the density of the balsa: lower density balsa has thinner cell walls that are more susceptible to buckling, whereas with thicker cell walls, the critical buckling stress is higher than that of kink band formations, which come about from rotational forces due to naturally present fiber misalignments [74, 75].

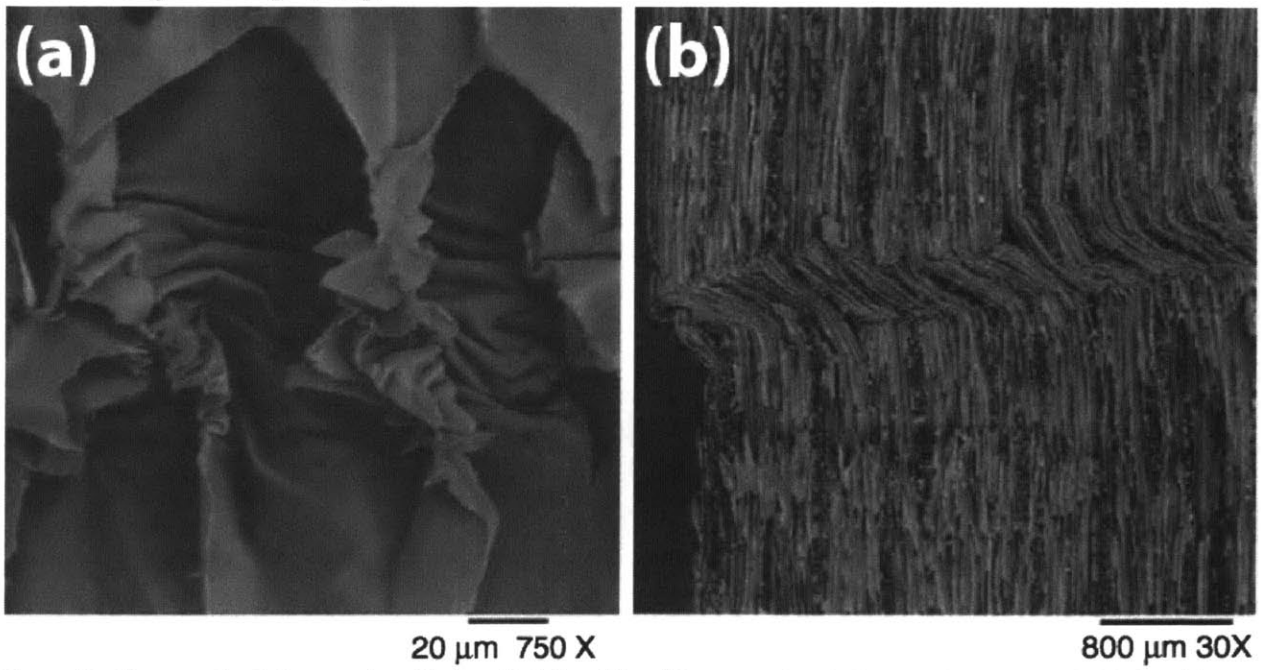

Figure 18: Compressive failure modes of balsa. (a) Cell wall buckling, prevalent in low-density, thin-walled balsa. (b) King band formation, prevalent in higher density balsa, due to inherent, natural eccentricities of cells with respect to the loading direction. Reprinted from [75] Copyright 2009, Springer.

The significance of this shift in deformation modes is evident in the energy absorption capacity of balsa, measured as the area under the stress-strain curves. **Figure 19** plots, per unit volume and per unit mass, the measured energy absorption capacity with respect to density for both quasi-static (0.0013 s^{-1}) and dynamic (3000 s^{-1}) straining. The S-shape of the data trend is due to the shift in deformation mode: when the mode shifts, at around 170 kg/m^3, the plateau stress for kinking does not increase with density as rapidly as it had for buckling. The result is a transient drop in specific energy dissipation, which is then again recovered for higher densities.

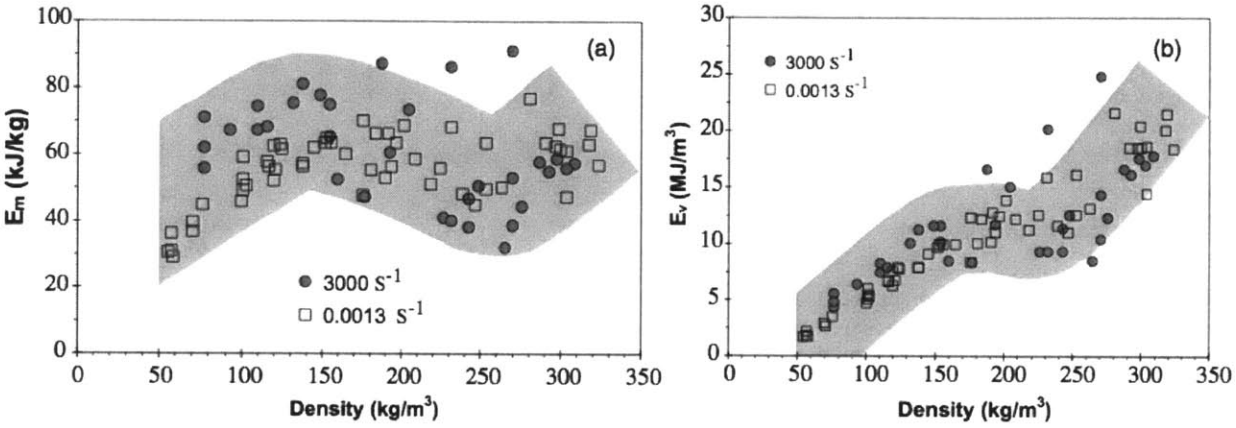

Figure 19: Variation in energy absorption capacity of balsa by density and strain rate per unit mass (a), and per unit volume (b). Reprinted from [74] Copyright 2003, with permission from Elsevier.

3: Mesoscale model of fibril-matrix behavior

In spite of extensive experimental work, relatively few simulation studies of wood mechanics have been reported. Some molecular dynamics simulations focused on the swelling, twisting, or self-arrangement of cellulose microfibrils [35, 37, 38, 56, 76-79] or on the elasticity of single chains [40]. There has even been some coarse-graining of the cellulose microfibrils [78], however, no model exists, to the best of my knowledge, that explores the wood polymer and fibril interactions at the mesoscale. While the properties of the cellulose crystals are certainly important, it is really the interplay between the fibrils and the matrix that governs the behavior of wood, and thus, it is the key scale worth investigating and understanding. The parameters at this scale, such as MFA, fibril lengths, and matrix composition and lignification influence the bulk properties, and by modeling this mesoscale, we can explore the effects of these parameters and identify the features that ultimately translate to wood's superior structural performance.

A fully atomistic model of a microfibril on its own is computationally expensive, to attempt to model, atomistically, many of these fibrils in a matrix of hemicellulose and lignin would be beyond impractical. Additionally, while the cellulose fibrils are consistent between species and types of wood, the composition of the matrix can vary greatly with different types of hemicelluloses and different lignin contents. Since it is the general behavior we are looking for, our first model must be a generalized simplification of the cell wall material with as few adjustable parameters as possible, while future models, informed by these first, simple models would incorporate more parameters, ultimately approaching a precise and accurate mesoscale representation of wood that could be used as inspiration for material fabrication or to direct and control the growth of wood.

The purpose of this study is to better understand the underlying mechanisms responsible for axial stiffness of different types of wood. The goal is not to specifically to recover quantitatively, the stress-strain behavior of specific wood species, but rather to simulate the mechanisms, common to all species of wood, that govern the trends in their mechanical behaviors. As such, any measure of force or stress, in relation to strain is sufficient to analyze the general behavior (rather than the specific strength and elasticity) that persists even after the measured value is mathematically manipulated to convert to bulk stress.

3.1 – Materials and Methods

Following the methods of previous successful coarse-grained simulations [4, 80-82], the initial attempts at modeling the cell wall mechanics were three-dimensional, and incorporated randomness in the geometry. These first simulations were fraught with issues and malfunctions brought about by poorly justified parameters and the heterogeneity from the random distribution over relatively few molecules. Further iterations of involved increasing the number of molecules in an effort to homogenize the model, however the simulations got larger and slower without any real progress. Efforts were then shifted towards removing the random elements, making the model homogenous to start, and then tuning the less defined parameters. The result of these efforts is a simplified, two-dimensional model, with parameters justified through literature that

allowed us to reproduce the expected behavioral trends common to bulk wood. The development of the model is guided by our desire to come up with a simple model that has the potential to probe interesting questions about the mechanics of wood at the cell-wall scale, and to develop a test bed to identify future experimental studies. The first iteration is designed to verify that basic model sufficiently mimics the expected stress-strain behavior, and then measure the effect of the initial MFA and how the angle changes with strain. With the same, verifying parameters, the geometry is then expanded for the second iteration of the model to measure the effects of various fibril lengths. Future iterations of the model can follow this same path of utilizing parameters that work and playing with the geometry to probe the effects of other parameters, matrix density for example. Additional molecule types can be added to account for various matrix compositions and lignin contents, and microfibrils could be allowed to fracture (in a manner guided by experimental results or atomistic simulations) to investigate material failure mechanisms. Regardless, though, of what could be simulated in the future, the simplified models here are the first steps.

3.1.1 – Model Formulation

The intent of coarse-graining is to model a large system of molecules in a simplified manner, to drastically reduce computation time while preserving the mechanistic origin of the deformation behavior and resulting mechanical properties. As the cell wall is constructed of what are essentially one-dimensional fibrils, the key features to replicate are the energies of the axial strain, bending angle, and cross-linking of the fibrils, expressing the total energy of the system as:

$$\square = \square_A + \square_B + \square_{link} \quad (1)$$

where $\square_A$ is the total axial strain energy, $\square_B$ is the total bending energy, and $\square_{link}$ is the total crosslinking energy. Similar techniques have been used effectively to model the behavior of carbon nanotube systems [4, 81].

The axial strain and bending energies are simulated through harmonic potentials of the form

$$\square_A = \sum_{bonds} \frac{1}{2} K_A (r - r_0)^2 \text{ and } \square_B = \sum_{angles} \frac{1}{2} K_B (\theta - \theta_0)^2, \quad (2)$$

where r is the distance between bonded beads and θ is the angle formed by three consecutive beads with the "0" subscript that refers to the equilibrium configuration. The inter-fibrillar interactions are modeled by a 12:6 Lennard-Jones (L-J) potential of the form

$$\square_{link} = \sum_{pairs} 4\varepsilon \left[\left(\frac{\sigma}{r}\right)^{12} - \left(\frac{\sigma}{r}\right)^{6} \right] \quad (3)$$

with ε as the energy at equilibrium and σ as the distance parameter for each pairwise interaction. With two bead "types" (one for the hemicellulose, another for the microfibril), a total of 14 parameters are included in this model (4 harmonic parameters K_A, r_0, K_B, θ_0 for each particle type, and the two L-J parameters, σ and ε, for each interaction type (microfibril to microfibril, microfibril to hemicellulose, and hemicellulose to hemicellulose). The properties of the hemicellulose, based on those of a single cellulose chain, as modeled atomistically by Wu, Moon, and Martini [40], with cross sectional area, A = 31.7 Å^2 and Young's modulus, E = 100 GPa, are related to the axial spring energy constant by

$$K_A = \frac{AE}{r_0} \quad (4)$$

Here, r_0 is chosen as 10 Å to represent the length of a single repeat unit (corresponding to 42 atoms) in the chain giving each bead mass, m = 324 amu. Each cellulose molecule is designed to represent a microfibril of 36 chains, using mass, m = 11,664 amu, area, A = 1,142 Å^2 and Young's modulus, E = 200 GPa, and using the same r_0 for the same repeating unit, K_A for the cellulose is calculated. The larger modulus of the same cellulose molecule is attributed to extra axial, inter-glucose hydrogen bonding that occurs while the chains are aligned within the fibril [40]; a Young's modulus of 200 GPa is reasonably within the range of accepted experimental values [44, 78, 83]. Lacking any substantial information on the bending rigidity of these molecules, values for K_B are estimated first for the microfibril, by considering the sum of the axial strain energies of the cellulose chains under a small bending angle assuming a linear strain distribution through the cross sectional area. For the purpose of this calculation the cross-sectional geometry of the crystalline microfibril is based on previous atomistic simulations [38, 41, 56, 77-79] and various imaging techniques including Raman spectroscopy [83], x-ray diffraction and scattering [39, 44, 83, 84], and solid state NMR [39, 44]. As there are multiple suggested geometries and potential bending axes, an approximate value or K_B is selected to use an appropriate order of magnitude for the simulation rather than a precise measure. To estimate K_B for the hemicellulose molecules, the previously calculated value is scaled down by the ratio of bending stiffnesses,

$$K_{B2} = K_{B1}\frac{E_2 I_2}{E_1 I_1}. \quad (5)$$

Here, the cross sectional moments of inertia are calculated for the cellulose as $I_1 = \sum A \cdot r^2$ where A is the 31.7 Å^2 of the single chain and r is the distance to the bending axis (based on the aforementioned geometries) and for the hemicellulose we assume a circular cross section with radius of 3.18 Å (such that the area is conserved) and use $I_2 = \frac{\pi r^4}{4}$. The interaction energy of a hydrogen bond in cellulose, determined through molecular mechanics [35], can be approximated by a 12:6 L-J potential with ε = 6 kcal/mol and σ = 2.5 Å. These parameters are used for the hemicellulose-to-hemicellulose interactions, representing a single hydrogen bond per connection. For the cellulose to hemicellulose interactions, we use a larger sigma in order to generate an energy landscape, from the perspective of the hemicellulose beads, consisting of a series of intersecting circular troughs each around a cellulose bead, creating a series of deeper wells at the intersections, spaced by 10 Å. This choice for σ is intended to emulate the relatively larger surface of the microfibril with respect to the hemicellulose, providing a continuous bonding surface along the length of the microfibril. The effective "depth" of each well is chosen to be equivalent in energy to three hydrogen bonds [25]. For the final interaction type of cellulose to cellulose, we use a low energy value and a large distance parameter solely for the purpose of maintaining the spacing between microfibrils. This approach is used to model the density of the inter-fibrillar matrix as well as moisture content and boundary conditions imposed by the cellular structure and cell wall layers, which serve this function.

These considerations led to the following numerical parameters. For the microfibrils:

m=11664 amu; K_A=3,286 kcal/mol-Å^2, r_0=10 Å; K_B= 50,000 kcal/mol-rad^2; θ_0 = 180°. For the hemicelluloses: m=324 amu; K_A=45.64 kcal/mol-Å^2, r_0=10 Å; K_B= 25 kcal/mol-rad^2, θ_0 = 180°. For the microfibril-microfibril interactions: σ =68.6 Å, ε = 1 kcal/mol; for the microfibril-hemicellulose interactions: σ = 8.9 Å, ε = 9 kcal/mol; and for the hemicellulose-hemicellulose interactions: σ = 2.50 Å, ε = 6 kcal/mol.

3.1.2 – Model Geometry: Variable MFA

The first version of the model is designed to be a very simple representation of the cell wall molecular interactions, and measure the effects of varying the MFA. The model consists of 10 cellulose microfibrils, each with 30 beads, initially arranged in the x-y plane at a chosen MFA (35, 40, and 45 degrees) with respect to the y-axis. The fibrils are initially spaced at a perpendicular distance of 77 Å [25] and the simulation box is periodic in the x-direction to simulate an infinite width. The hemicelluloses, each containing 36 particles, are placed initially as and cosine functions with amplitudes of 36.5 Å (to span the inter-fibrillar space) and varying phase along an axes parallel to cellulose molecules, in order to encourage the formation of the bridges and loops between microfibrils, believed to play the key role in this mechanism [25]. Four hemicellulose molecules span every gap and four are centered over each microfibril to provide extra connectivity that are not directly bridges or loops —this number can be adjusted, in principle, and could be used as a parameter to represent different hemicellulose to fibril ratios.

The celluloses are confined to the x-y plane for the entirety of the simulation, however, in order to avoid any singularity type effects from restricting the more flexible, and inherently more motile, hemicelluloses to entirely planar motion, those molecules are permitted to move in three dimensions to allow them to more freely wrap around and/or cling to the celluloses. The beads that are clamped for the tensile test are alternated between the tops and bottoms of adjacent celluloses; this way, upon pulling, each cellulose molecule can shear away from the other two that are adjacent to it. The geometry of this model is designed to focus on the inter-fibrillar shearing along the length of the fibrils. The purpose of this limitation is to confine the scope of the results to the most basic level of the wood polymer interactions. A larger and/or three-dimensional model could include effects from longer interaction lengths or more random and realistic distributions of fibril lengths to more precisely simulate the cell wall material. However, the simplified setup as described is sufficient for simulating the basic interactions of the wood polymers and their contribution to the deformation behavior of the material as reflected in the resulting force-displacement curve. The simulation is equilibrated first by restricting vertical motion of the clamped beads and running the simulation while allowing the box length in x to adjust to follow the contraction and keep the material infinitely continuous along x. We then run it again with the box length fixed and the clamped beads free to relax in the vertical direction and then apply an energy minimization, in order to reduce any residual axial force in preparation for the tensile straining. Throughout the equilibration process, a viscous damping parameter of 100 Kcal/mol-fs is applied and the completion of each phase of equilibration is observed through the simulation visualization once all visible motion has ceased. A close up of the equilibrated model in the context of the cell wall structure is shown in **Figure 20**. Once equilibrated, the

aforementioned clamped beads are pulled at a constant strain rate of 0.05/ns up to a total strain of about 40%. The vertical component of the force on each bead and the mean vertical distance between the top and bottom clamped beads are recorded as averages over intervals of 0.01 ns.

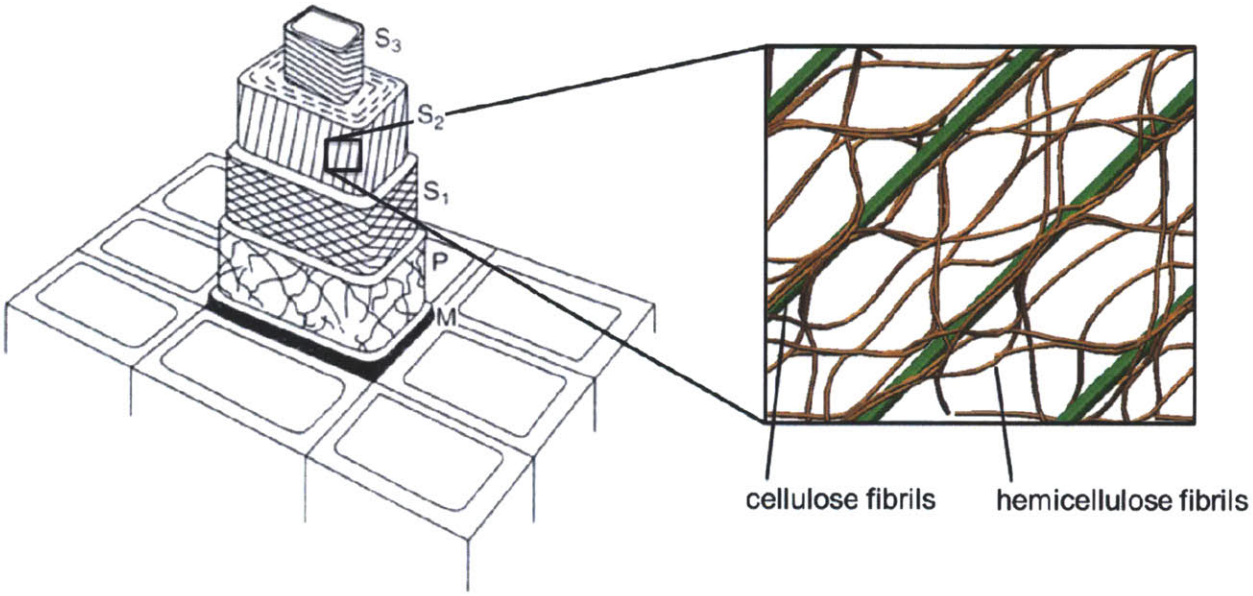

Figure 20: Schematic of cell wall layers within cellular structure (image reprinted from [10] Copyright 1998, with permission from Springer), and a depiction of the mesoscale model used here, representing cellulose microfibrils (green) interconnected by hemicelluloses (brown). The cellulose microfibrils are much stiffer than the more flexible, less ordered hemicellulose molecules, which provide a matrix of connections between microfibrils.

While the inter-fibril spacing in this simulation is based on a measured value, the single-molecule representation of the microfibrils does not account for their relatively large thickness when considering the cross sectional area of the simulation box, measured as parallel to the *x-z* plane. This unrealistic area, in addition to the unrealistic density of hemicelluloses makes any measure of stress based on the *x-z* simulation box area unreliable. What can be measured though, is the force per microfibril, and with a known (or chosen) value of microfibril density per cross-sectional area, a stress-strain relationship can be approximated. However, such a quantity would be a variable of wood species, wood type (normal, tension, reaction, etc.), and even moisture content, and in all cases, the stress is simply a scaled measure of force. As such, the force-strain relationship is a sufficient means of qualifying the mechanical behavior and chosen here as a primary means of analysis.

3.1.3 – Model Geometry: Variable Fibril Lengths

The second version of the model is designed to measure the effects of varying the lengths of the fibrils. Here, all geometries (with fibrils of 12, 20, 30, 40, 60, and 100 beads) are contained by the same sized simulation box, which means that the geometries with smaller lengths contain more fibrils to fill in the same box size. The fibrils are, again, initially spaced perpendicularly by 77Å, and are arranged at a MFA of 45°. Consecutive fibrils along each 45°-

vector overlap only slightly while adjacent fibrils are shifted along the parallel vector so that the adjacent fibril overlap by about half their lengths. **Figure 21** illustrates this arrangement for geometries of two different fibril lengths after equilibration.

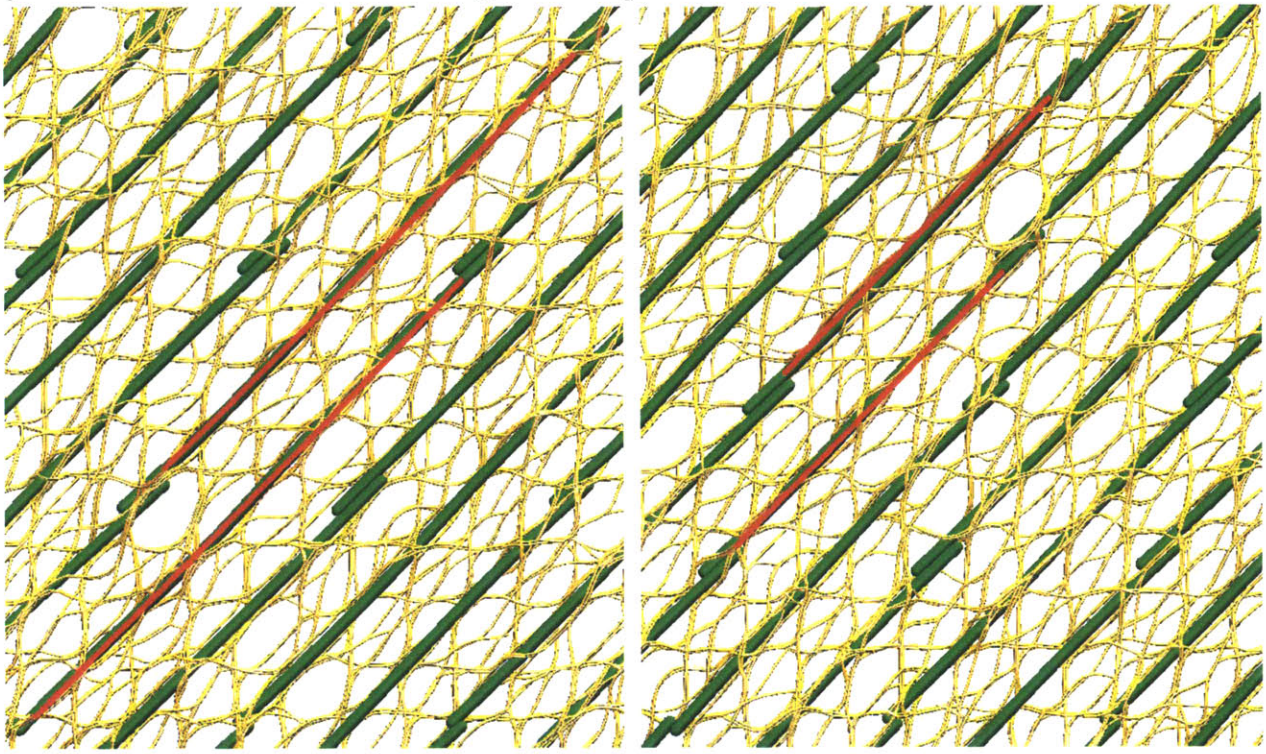

Figure 21: Equilibrated geometries of the sixty bead fibrils (left), and the forty bead fibrils (right). Pairs of adjacent fibrils are highlighted in red to illustrate the half-length overlap geometry as described in the text. All length iterations are embedded in identical hemicellulose matrices.

The hemicellulose density and equilibration procedures are the same as in the first version of the model. In this version, however, instead of pulling on individual beads and measuring the force of the pulling, we clamp entire regions at the top and bottom of the box, including the hemicellulos beads, and measure the average stress-per-atom in the unclamped region. The reason for these differences is that in this more complex geometry, dynamic effects could be more pronounced. Pulling on individual beads produced drastically different behaviors in the smaller length iterations, where the short fibrils would simply be pulled out of the top or bottom of the geometry without invoking any of the expected mechanisms in the middle, and dropping the measured force to zero before any significant strains could be achieved. By clamping regions instead of individual beads, the isolation effects on individual fibrils are removed and the entire geometry is deformed more homogenously regardless of fibril length. Measuring the stress-per-atom is simply a consequence of this altered pulling method, and the same argument applies: that it is the trend that is being measured, rather than the absolute values.

3.2 – Results and Discussion

3.2.1 – Variable MFA

The force-strain behaviors as described above for the iterations of the first version of the model, each with different initial microfibril angles are plotted in **Figure 22(a)**. Visible in all three plots are the three regimes of the tensile behavior of wood: the initial, purely elastic region, which transitions, post-yielding, to the less stiff plastic region, and, at higher strain values, the material stiffens as the fibrillar orientation approaches vertical. The additional data plotted in **Figure 22(a)** are representative stress-strain diagrams of isolated wood fibers (single cells) as obtained from experiment of four wood species with MFA ranging from 30-45° [85]. The experimental results were obtained at a length scale many orders of magnitude higher than that of the model, however the behavioral comparison remains valid as the properties of a tubular cell loaded along its axis scale linearly (by the solid to void ratio) with the properties of the cell wall material [11]. The anisotropy of the cell wall material is known to manifest at the cellular level as induced torsion due to the 'unwinding' of the helical fibrils [22, 26], however this effect does not come into play in terms of the axial mechanical behavior of an isolated cell. Furthermore, compression of micropillars carved out exclusively of the S2 layer demonstrate that the characteristic elastic-plastic response of wood at the bulk, tissue and fiber (cellular) scales is also present at that of cell wall material [86]. **Figure 22(b)** shows how the instantaneous MFA decreases as the model strain is increased. This MFA-strain relationship is in good agreement with experimental measurements and the linear approximation,

$$\mathrm{MFA}(\epsilon) = \mathrm{MFA}(0) - \cot\left[\mathrm{MFA}(0)\right]\epsilon, \tag{6}$$

based solely on geometrical considerations [12, 17, 27, 62]. In addition to simulating the general behavior of cell wall material, the mechanics of these models also reproduce the trend of increasing stiffness with decreasing microfibril angle, as observed in experimental studies [23, 26, 85, 87] and described mathematically [25, 62, 85]. The molecular structures of the microfibrils and hemicelluloses, from which this model was derived, suggest a slip-stick behavior between cellulose and hemicellulose, where when the shear strain between two fibrils reaches a critical value, the hydrogen bonding ceases to overpower the internal stiffness of a stretched and bent hemicellulose. The molecule wrenches free, relaxes, and then re-attaches at a new location along the fibril. A single slip event reduces the average tensile force in the model without reducing the strain, but immediately after the slip, the hemicellulose continues again to contribute its stiffness to the bulk exactly as it had previously, so before and after a slip, the force per strain increments have the same value, while the absolute force experienced a near instantaneous decrease.

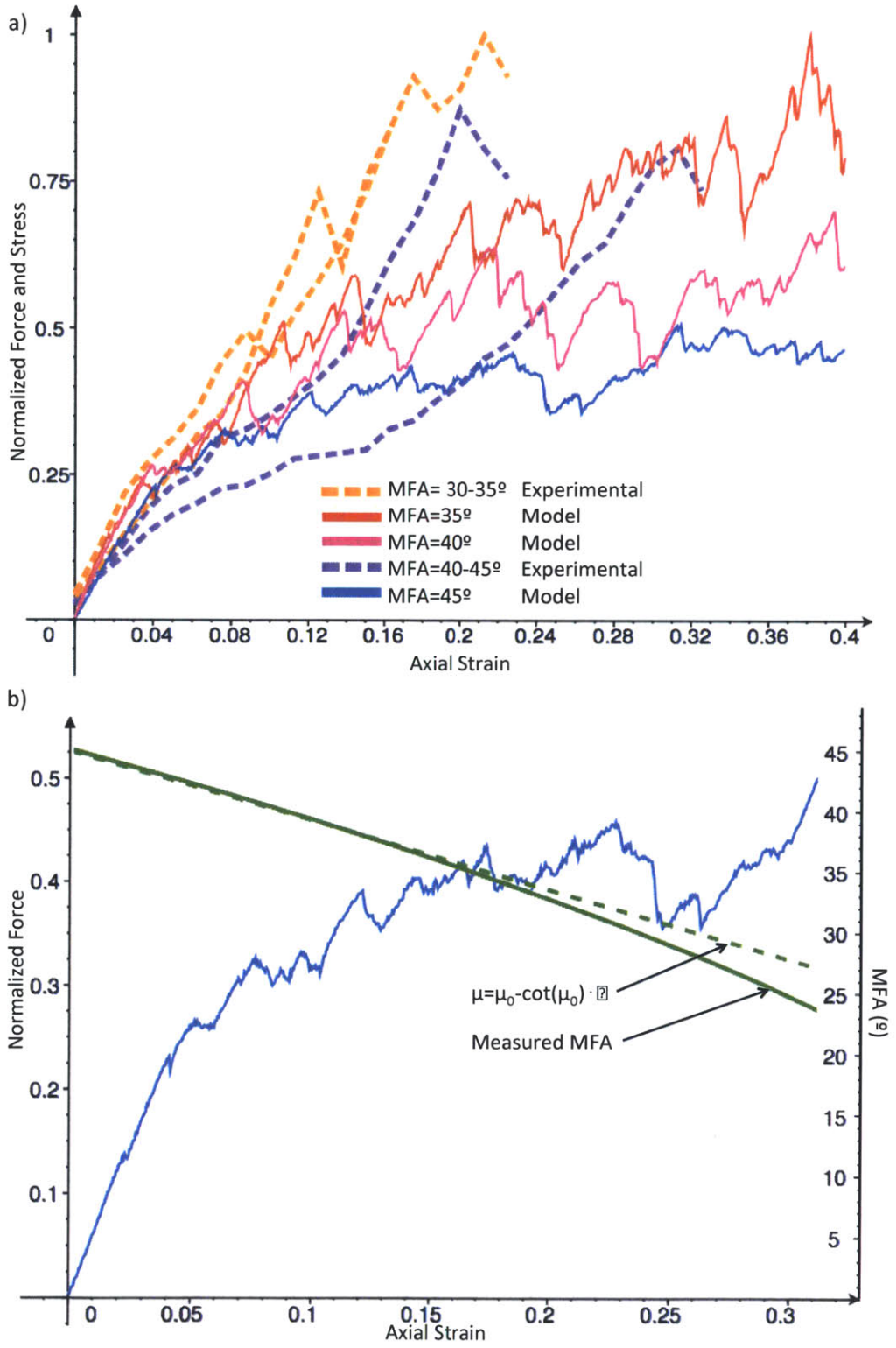

Figure 22: Force-strain results and analysis of microscopic mechanism. (a), Simulation results for three different microfibril angles and representative single cell stress-strain behavior of four different wood species (reproduced from [85]), each showing the three regimes of behavior: Elastic, Slip-Stick Plastic, and high strain stiffening. (b), Simulation results for the 45° MFA model with the average MFA as calculated from the simulation and the linear approximation of MFA-strain behavior based solely on geometry.

As the deformation behavior is a dynamic process, the rate of strain can affect the magnitude of the measured forces [88]. While beyond the scope of this study, the extreme cases can be qualitatively addressed. In the pre-yielded elastic behavior, the model is essentially an inertial spring that when stretched sufficiently slowly, will act as a massless spring, with some constant force-displacement value, K. If stretched rapidly, however, rate effects may produce an inhomogeneous distribution of strain along the length of the spring, with the larger magnitude of strain skewed towards the end that is being pulled, and in the case of this model, where the force is measured at the pulled ends of the fibrils, a higher strain rate would increase the magnitude of the measured force. Both of these extremes also apply to the post-yielded behavior, however in addition, each individual molecule can be considered as an inertial spring, which may further increase the recorded forces under higher strain rates. Furthermore under a sufficiently low strain rate, a hemicellulose molecule may detach from the cellulose fibril at a larger strain (as the dynamic effects that tend to induce earlier separation would not be present), which could result in a larger snap-back before reattaching, potentially increasing the magnitude of the saw-tooth behavior of the plastic response. Future studies should address the significance of the effects of strain rate on the mechanical response of the cell wall material.

The initial stiffness of the model, as seen in the plots in **Figure 22**, is the sum of the stiffness contributions of every individual hemicellulose molecule, because in that region of small strain, there are none, or only a few slip events. After yielding, there is a nearly continuous flow of slip events, effectively simulating the "softer" response—plastically straining the material without damaging it [12]. The experimental stress-strain diagrams of the fiber level shown in **Figure 22(a)** exhibit the same three-regime behavior, though over a smaller range of strain. Results from that same study also include stress-strain diagrams of the same wood species at the bulk level, and there, again, the same three regimes are present, however over an even smaller range of strain. These results suggest that, while fundamentally, the mechanism we model is responsible for the mechanical behavior, the higher levels of hierarchy increase the strength and stiffness at the cost of extensibility.

In our model, slip events, exactly as described above are shown in **Figure 23(a)**, and in addition to the slippage along a microfibril, hemicelluloses can also slip with respect to each other, within the inter-fibril space, shown in **Figure 23(b)**. These minor slip events in effect represent the hydrogel-like behavior of the hemicellulose matrix [12], and with a denser, and three-dimensional, hemicellulose mesh, it is likely that said behavior would be more prevalent, potentially resulting in a smoother force-strain behavior than the sort of saw-tooth like plots depicted in **Figure 22**.

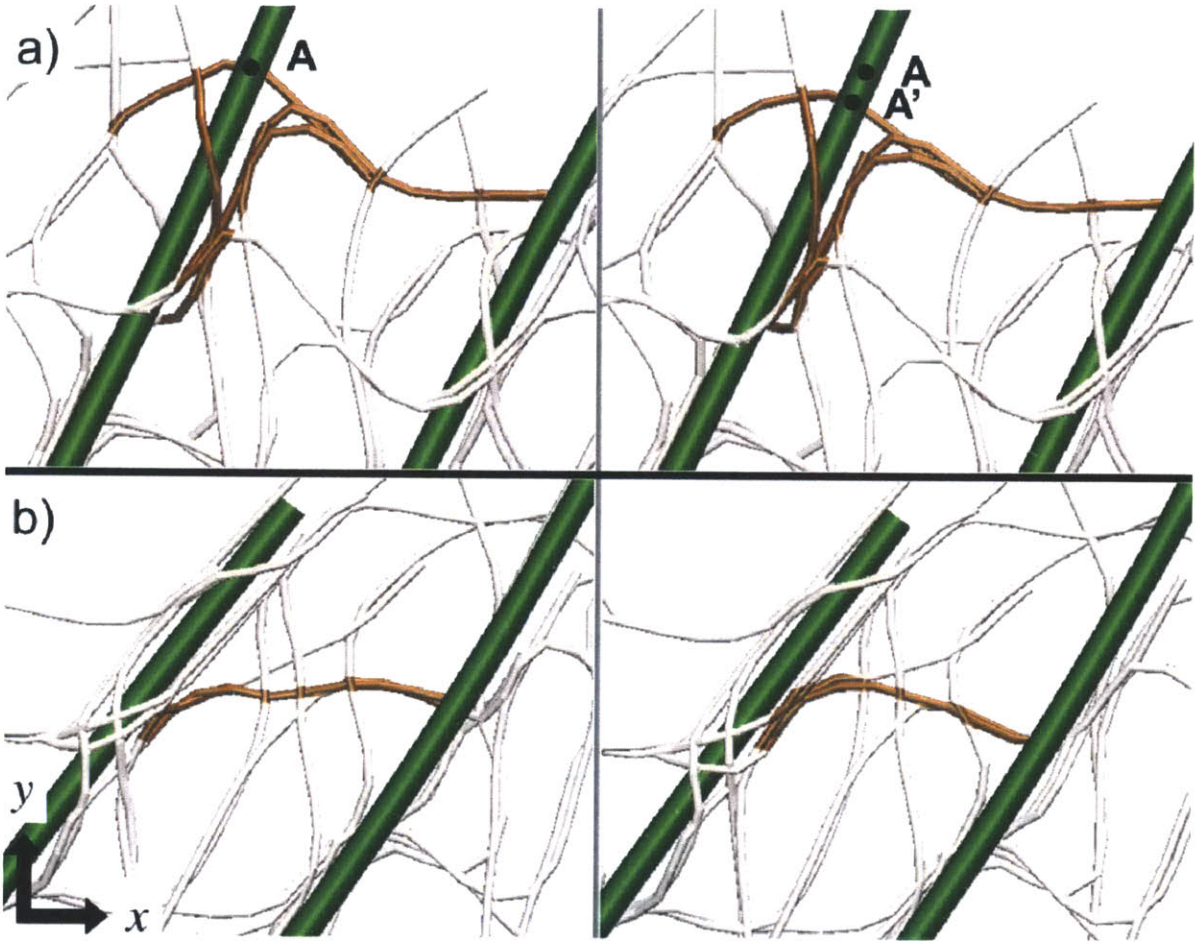

Figure 23: Molecular mechanism of deformation. Observed slip events: (a), A group of hemicelluloses translates downward along a microfibril. Point A highlights the location of the hemicelluloses before the slip (left) and Point A' shows the vertical location to the next snapshot taken after the slip has occurred (right) (b), A segment of a single hemicellulose relaxes in the inter-fibril space, adjusting its connectivity to other hemicelluloses within the matrix, made visible through a clear change in shape. Both events are examples of relatively large reductions in the overall axial stress over small strain increments, and a continuous flow of such events effectively reduces the overall stiffness in the post-yielding plastic strain regime. Each slip event results in irreversible deformation without damaging either the cellulose microfibrils or the hemicelluloses.

In wood, the space between fibrils is completely filled with this hemicellulose (and lignin) matrix, which, in addition to inter-connecting adjacent fibrils, also acts as a solid, or semi-solid barrier, maintaining the separation that, in our simulation, is imposed by the microfibril-microfibril L-J potential, preventing aggregation. It is possible that in wood, the thickness and density and general disorder of the hemicellulose matrix would be sufficient to reduce the internal slipping and make it so the only slippage occurs with respect to the fibrils. It is also possible that the opposite could occur, and the mesh might constantly adjust internally, maintaining its integrity, while allowing the individual molecules to relax during straining. The fact is that the exact governing mechanism is not precisely known, as it cannot be measured. Some suggest that the hemicelluloses cling to the fibrils, and the inter-fibrillar interactions consist mainly of the meshes around each fibril interacting with each other [4, 12, 17, 62], while others suggest that the interaction consists mainly of individual hemicelluloses actually spanning

the entire gap between fibrils [22, 25], forming bridges and loops that slip against the fibrils, both of which are represented in our model. The experimental results are limited to a far larger scale than the mesoscale model used here [85, 87, 89], and existing analytical descriptions consider the hemicellulose matrix as continuous material [27, 63, 65, 90].

The fact that our model correctly reproduces features of the force-strain behavior of wood implies that polymers that behave and interact as we have programmed them (which is a simplification of how we know they behave and interact) will deform as predicted in the literature, and exhibit the expected stress-strain characteristics of wood cells and bulk wood. Our model displays hydrogel relaxation, as the most frequent mechanism of irreversible deformation, however, depending on any number of parameters, such as the amount and/or arrangement of hemicellulose (which could be adjusted to create various states of pre-stress), the lengths of and spacing between microfibrils, and the effect of moisture content on the elastic and interactive parameters, any of the observed mechanisms might prevail over the others. A better mimic of the behavior, arrangement, and interactions of specific wood polymers, would merit a more definitive assessment of the distribution of deformation mechanisms.

3.2.2 – Variable Fibril Lengths

The stress-strain relationships of the six iterations of the second version of the model are plotted in **Figure 24**. As this version is basically a geometric adjustment of the first version, the previous discussion of the mechanisms apply here as well, and, as expected, the three regimes of tensile behavior are clearly present. The elastic regions, and the immediate post-yielding regions show little, variation between iterations, at higher strains, however, a clear trend emerges: the longer fibrils show more pronounced strain-stiffening. As discussed previously, this third regime is due to the decrease in MFA as the cell unwinds, which was measured in the first model version plotted in **Figure 22(b)**. Observed in the simulation visualizations, applying strain results in both a decreasing of the MFA and a separating of consecutive fibrils. As consecutive fibrils are pulled apart, the overlap length between adjacent fibrils is reduced; for the shorter fibril iterations, the overlap diminishes almost entirely, whereas the longer fibril iterations maintain the overlap over larger strains, which allows the aforementioned stiffening behavior to manifest.

In the first version, the adjacent fibrils aligned over their entire 30-bead lengths, and by shearing them apart, they were pulled out of the hemicellulose matrix. Here, in the second version, there are fibrils that are completely surrounded by the hemicellulose matrix and by more fibrils, making it a more complete, yet still vastly simplified, representation of the cell wall material. Material failure, in this case, is categorized by a complete separation between the top and bottom clamps as shown in **Figure 25**. That our samples were able to completely separate into two completely separate pieces while not allowing the individual fibrils to fail suggests that it may be possible that actual wood cells may fail and fracture without actually fracturing the cellulose fibrils. This suggestion, however, cannot be drawn as a definitive conclusion, further studies should, in addition to improving accuracy, measure the strain of the cellulose fibrils and/or allow the harmonic bonds to break at some critical strain that should be based on either experimental evidence or fully atomistic models.

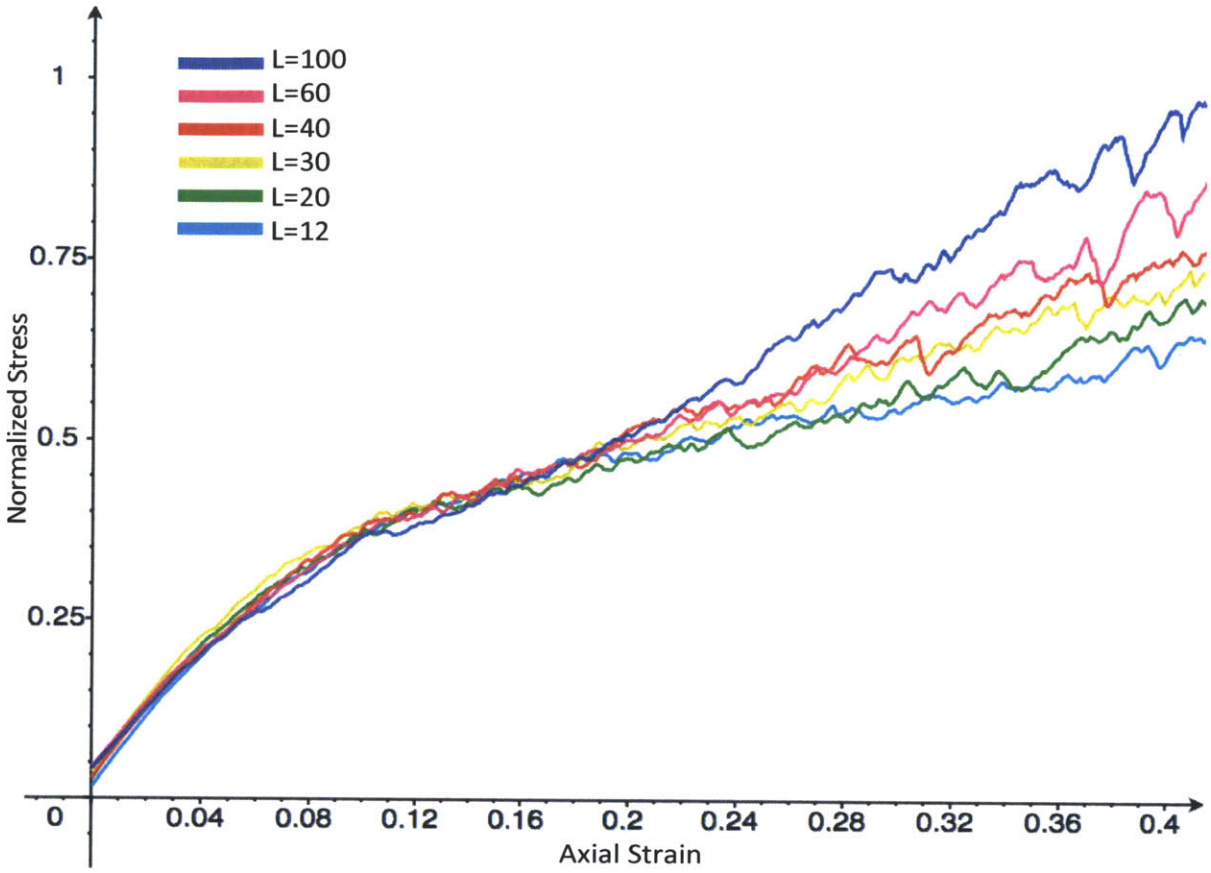

Figure 24: Stress-strain plots for model of various fibril lengths. At low strain, there is little variation, however at around 20% strain, the plots begin to diverge. The characteristic strain stiffening effect is more pronounced in the models of greater fibril length.

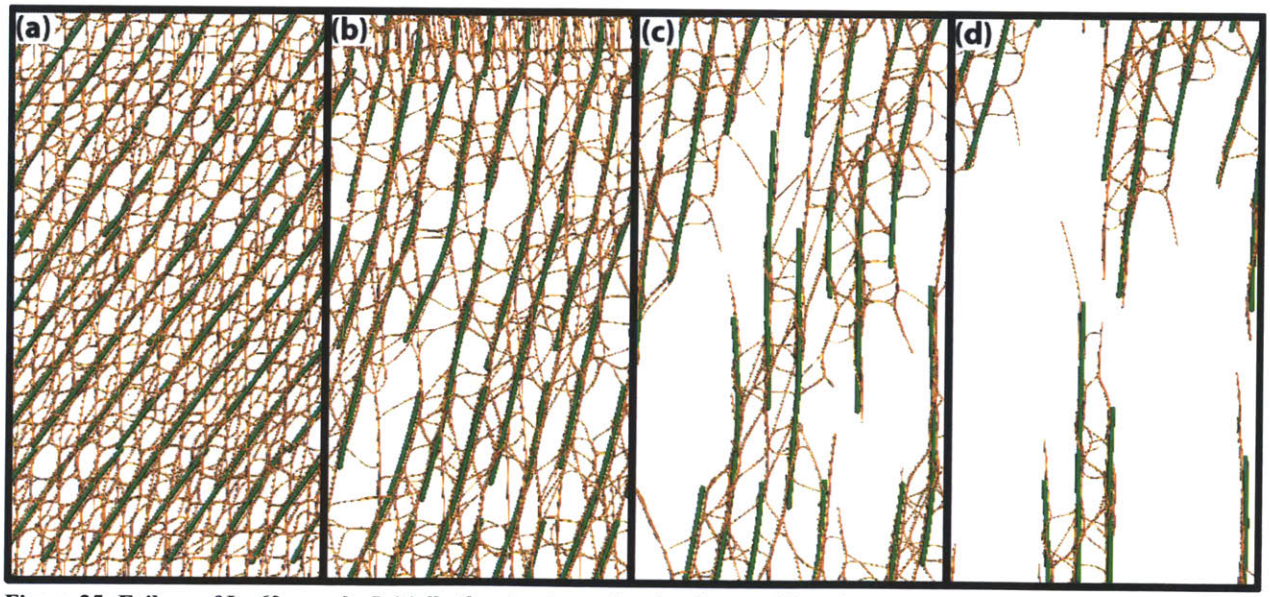

Figure 25: Failure of L=60 sample. Initially the structure, shortly after equilibration, is complete and connected (a). The space between adjacent and consecutive fibrils increases, as the sample is strained beyond 40% (b). The halves are mostly separated, only a narrow section of fibrils and matrix still span the sample (c). Complete separation is achieved; there is no longer even a single series of hydrogen bonds connecting the two halves (d).

4: Biomimetic Composites

The logic behind composite materials is to allow a combination of materials to achieve an ideal balance of strength, elasticity, and toughness that neither of the constituents could achieve on their own. Much of the natural world functions on this logic, as evidenced by its ubiquity in the bones of every vertebrate, in the cell walls of all plant life, and in many other life forms [5-7, 91]. Wood serves as an excellent example of what a composite material can achieve; it can demonstrate a massive range of structural properties between wood species and types that are essentially identical, chemically. By varying the arrangement and relative density of the constituents of the cell wall, plants can fine tune the properties of the wood that they grow to best handle the specific loading conditions [68].

As three-dimensional printing becomes more accessible, the fields of practical applications become more expansive [92-96]. With precisely manufactured print nozzles and special 'inks' 3D printers can deposit material, layer by layer, to build material of a specified geometry. Initially, these printers were massive and expensive, and limited in printing material; novel uses included highly detailed chess pieces [97], or 3D models of Escher's impossible structures [98]. With advancements in printing technology comes a wider range of theoretical application. The private space company Deep Space Industries plan to use an advanced 3D printer to assemble, in microgravity, structural grade metals from the raw materials mined from asteroids [99], and NASA is theorizing 3D printing a moon base out of the native rocks and soil [100]. With newly developing inks, of varying mechanical properties, and printing resolutions that are progressively increasing, the fabrication and fine-tuning of composites is becoming feasible for practical purposes.

In previous work by Leon Dimas in the Lab for Atomistic and Molecular Modeling (LAMM), computer models were designed to investigate the toughness of a bone-like topology of stiff and flexible material in a 'brick and mortar' like geometry [7]. The model geometry was then used as a template for a 3D printed composite of stiff and soft material, which is then mechanically loaded to fracture. This flow of this research is detailed in **Figure 26**. The stress distribution in the model is easily measured as an output of the simulation, whereas for the printed sample, it must be measured indirectly through observation of localized strains and fracture mechanisms. In another paper, we compared the mechanical behavior of the sample with that of simulation via stress-strain data and macro scale observations [8]. Here we further explore the deformation and failure mechanisms using microscopy on the post-fractured sample. Our purpose is to assess the viability manufacturing a composite material with properties that we specify beforehand via computer simulations further advancing the field of artificial and biologically inspired functional composites.

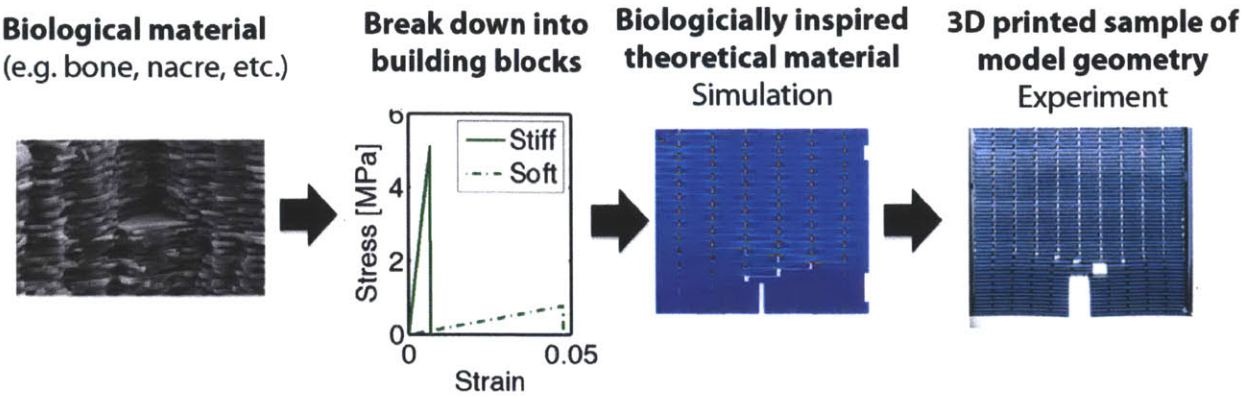

Figure 26: Flow chart summary of previous bio-inspired simulation and experiment. Adapted from [8] with permission.

4.1 – Methods

Optical Microscope

Observations under an optical microscope were made at 40x magnification. The specimen was lighted from both above and below in order to effectively highlight the surface features and distinguish between material phases. The optical microscope image can focus only over a very narrow depth range, making it an effective tool for surface features and defects; it is ineffective, however, in observing the fracture surface (the cross section of the sample).

Scanning Electron Microscope

To better examine the fracture surface, as well as quality of the printing, we use a JEOL model Scanning Electron Microscope, JSM-6610LV. A low vacuum setting is utilized so that charge buildup can be dispersed and a clear image can be attained without the requirement of coating the sample in gold. The sample is investigated at relatively low magnification (30x) in order to corroborate with the optical microscope observations. Higher magnification investigation (250x – 1000x) is used to investigate the quality of the 3D printed material: whether fracture occurs along the interface between the two material phases or independent of it, as per intent. The images were obtained from backscatter electron detection; the accelerating voltage and working distance are listed per individual image on the bottom bar.

4.2 – Results and Discussion

A snapshot of the simulation being strained is shown in **Figure 27**; key features highlighted are: near zero-strain region near notch, network of strain distribution away from crack, and strain concentrations near the crack tip, and **Figure 28** shows these regions highlighted in a photo and as seen at 40x magnification under the optical microscope. Under a macroscopic observation, visible in **Figure 28(a)** of, there is little, if any evidence of the far-field strain pattern, however the microscopic images of those regions, **Figure 28(a)** and **(b)**, reveal the difference. Compared with the low strain region near the sawn notch, there is a clear pattern of damage in the far-field region, indicative of the strain pattern of the simulation. In **Figure 28(d)**, the extra damage due to stress concentration is shown as complete separation of the soft material; also, the damage follows a path around the corner of a brick like the strain concentration in

Figure 27(c). The 30x magnification SEM image in **Figure 29** more clearly displays the topography of the cracks, such that the depth can be seen.

The location and direction of the cracks provide insight into the strain and fracture mechanisms. As the specimen is strained, and the stiff platelets are being pulled apart, the soft material is strained in two separate ways: Within each longitudinal row, the soft phase between bricks fails completely as it is pulled in nearly pure tension, while the soft material between rows undergoes shearing rather than pure tension, which induces tension along diagonals. The excessive tension manifests as cracks that form perpendicular to the direction of tension. The diagonal direction reverses at the junctions, with the indicative cracks as in **Figure 28(b)**.

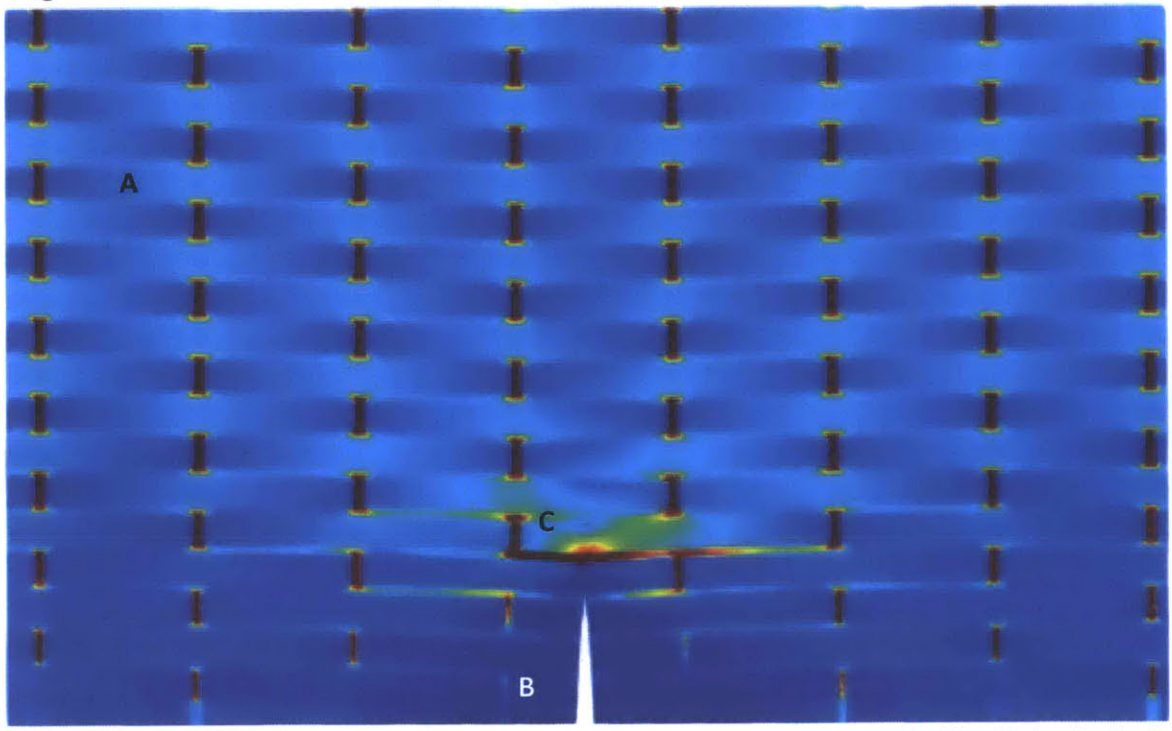

Figure 27: Longitudinal strain field, predicted by computer simulation mode I fracture loading. Notice the far-field strain pattern (A) consisting of regions of massive strains in interconnected by narrower, but still distinguishable slivers of higher strain, indicitive of the soft material's goemetric distribution. The stiff "bricks" are also distinguishable by lower overall strains, though relatively larger at mid-length. (B) denotes a region of nearly zero-strain, and (C) denotes strain concentration patterns—larger strain in the slivers of soft material, and far larger than usual strains in a brick. Adapted and reprinted from [7].

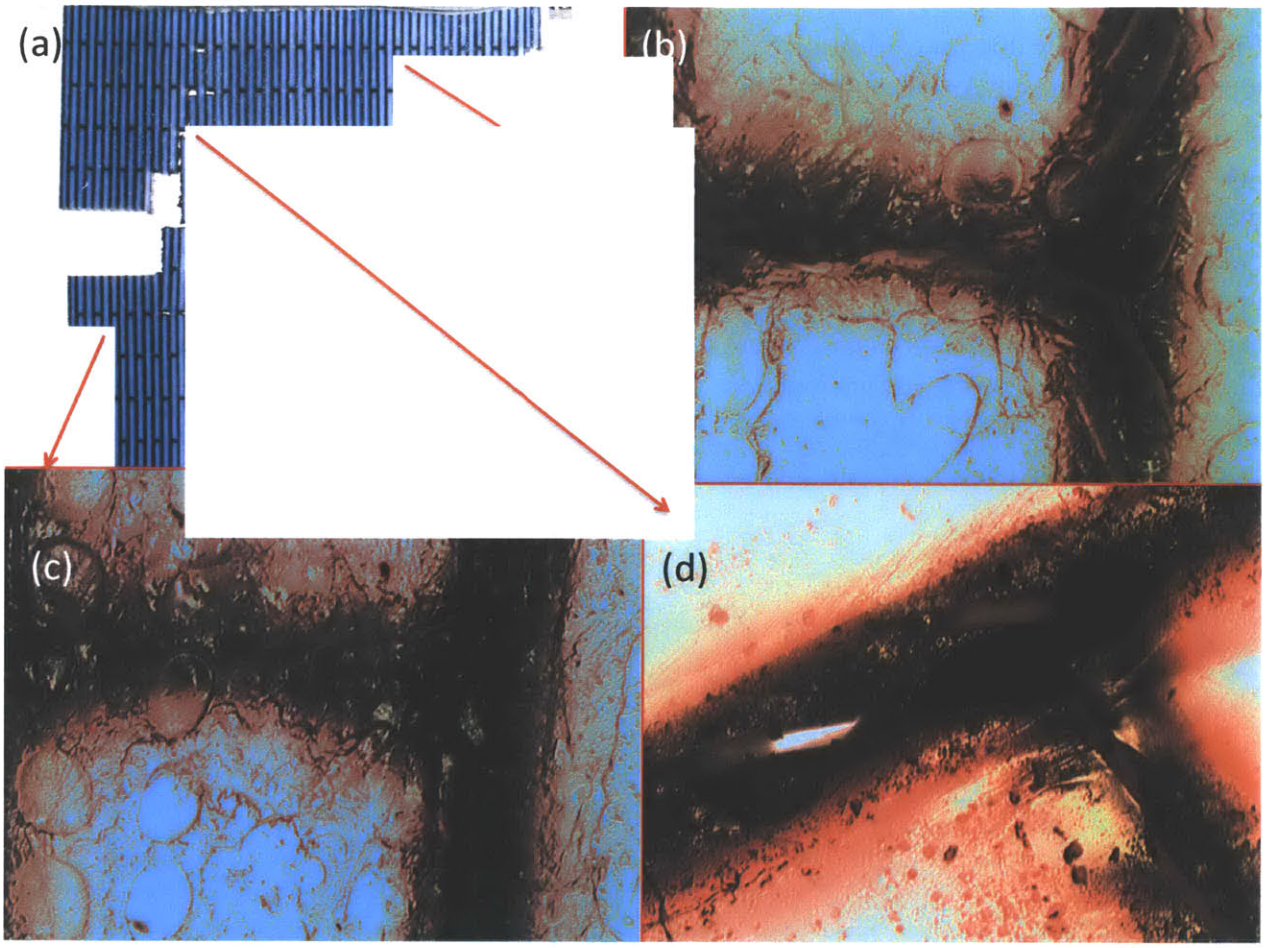

Figure 28: (a) Macroscopic image of fractured specimen and 40x magnified microscopic images of (b) the far-field damage pattern, (c) the undamaged region near the notch, and (d) damage near, but off of the crack path. The far field damage visible in (b) is indicative the mechanism of delocalizing stress from the crack tip, which, not only dissipates energy, but also helps direct the crack near the tip. In (d), the damage is greater than in (c), because the stresses are larger near the crack tip, but the damage is still limited to the soft phase, which forces the crack to round corners. This damage shows that the main crack actually split and propagated in multiple directions—only one of which was selected to continue through the rest of the material—dissipating more energy than a single continuous crack.

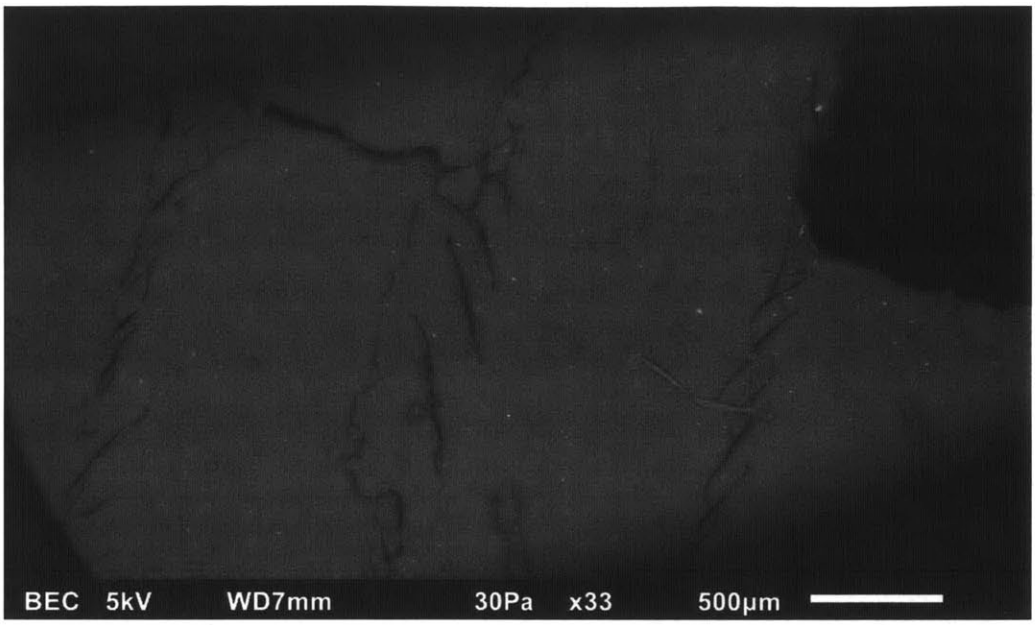

Figure 29: Low magnification SEM image of damage features depicted in Figure 28. Here, the diagonal cracking and deep fissures are more clearly visible, however the different material phases are not at all identifiable; we see in Figure 28 that this damage is limited to the soft phase. The diagonal cracking near the fracture path (top right) is messier, indicative of greater, less ordered damage resulting from excessive stresses before and during fracture propagation.

While the damage observed under the optical microscope shows no indication of interfacial failure between the two material phases, a higher magnification investigation is warranted. **Figure 30** shows successive close-ups of the fractured surface. The damage along the failure path is excessive and messy, however even under high magnification, there is no clear interfacial failure: it would appear that all of the fracturing occurs within the soft phase. In **Figure 30(b)** and **(c)**, there is visible stratification. This is an artifact of the layer-by-layer fabrication process. That these layers are visible implies that the material does not behave completely homogenously, meaning that the fabrication process has some impact on the material behavior. This detail, though significant in general, does not affect the composite behavior being investigated in that the geometric details of the constituent materials are at a much larger scale than the lamellar structure within each material. Were we to print a geometry that is closer to the resolution limit of the printer, it is likely that fabrication artifacts may be more prevalent.

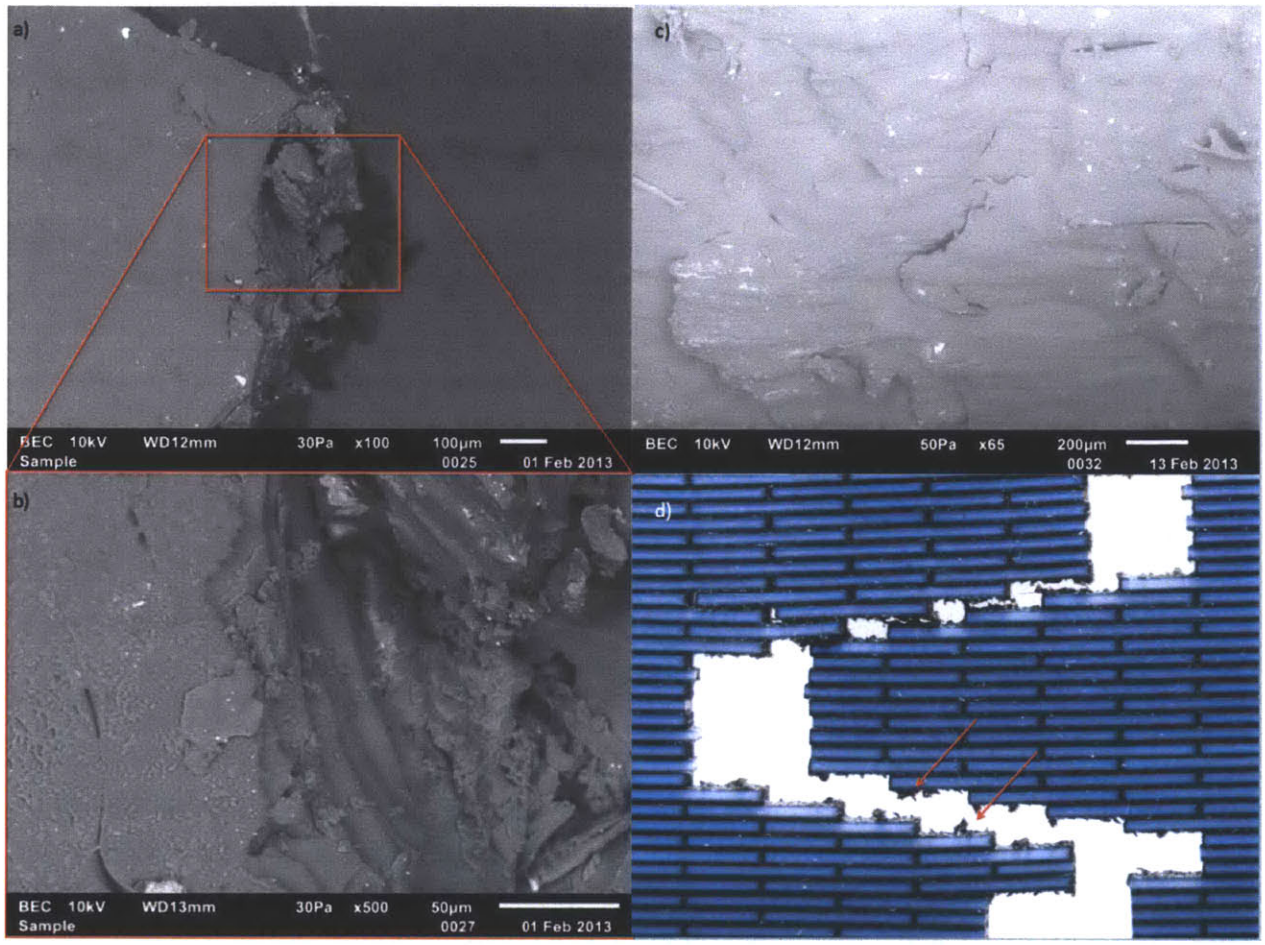

Figure 30: Evidence against interfacial failure. (a) Image of a rounded corner showing roughness with no clear interfacial de-bonding. (b) Close-up of highlighted area from (a): again, no clear interface failure, also visible is the layered composition of the sample, an artifact of the printing process and on a far smaller length scale than the main fracture (d) Macro-scale image of the fractured material with arrows indicating the "messy" failure of the soft phase.

5: Conclusion

The natural world has been successfully building tall and resilient long before mankind even thought to, much less develop a science for. Wood and stone, the first building blocks, were taken directly from nature, performing nearly as they did in nature. So, taken for granted that these materials work—and that we, having quantified their properties, we can use them relatively efficiently—there seems to be little reason to ask the question of why they work. However, in mankind's quest to understand the universe, the questions do get asked, and it turns out that nature has plenty to teach us. In Chapter 2.3.1, we compared a mechanism used by trees for vertical stability to the outrigger system used in tall buildings. Mankind likely developed this system likely independent of inspiration from trees, however the system had been developed through natural evolution. Are there other artificial innovations that share profound similarities with naturally evolved mechanisms? Nature tends to achieve much with little, and the logic and order of the natural world should continue to serve as a source of inspiration for artificial structures and materials [4-7, 91, 101].

The mesoscale models of this research are focused on the cell wall material because it plays the key role in modulating, among other properties, the stiffness of wood, and understanding the mechanisms in play is the first step towards controlling or reproducing them. Though a vast simplification of the molecular structure of the S2 layer of wood cell walls, our mesoscale models, developed to reproduce the generic behavior of the nature of the molecular types and their interactions, qualitatively reproduced several definitive properties of the mechanical behavior of the cell wall material. We have shown that the three-regime behavior as well as MFA dependence is properties that are indeed derived from the inter-fibrillar shearing. With the viability of this technique confirmed, we have, in a simplified manner, explored the effects of varying fibril lengths to develop a reasonable relationship to the mechanical behavior. Our second model also provided a potential insight into the fracture and failure of wood cells as the sample could undergo complete failure without allowing the fibrils themselves to fail. And further, we have opened the door to more in-depth studies are now possible. In future work, atomic scale models could be utilized to more precisely choose the less understood parameters of our model such as the bending stiffnesses and the energy of the L-J potentials; a denser matrix of hemicelluloses to not only span, but also maintain the inter-fibrillar spacings rather than the artificially imposed microfibril to microfibril large-σ L-J potential. Additionally, the fracture and failure mechanisms of either the bulk material or the individual molecules could be explored with future, specialized variations of this modeling technique. A more detailed molecular model could incorporate constraints imposed by higher levels of hierarchy (to describe fracture and plasticity), and simulate how the inter-fibrillar shearing that is described in our model is invoked by straining those higher structural levels and thus make reasonable predictions concerning the behavior of wood or structurally similar materials.

The cell wall material, by exhibiting a wide range of stiffness and toughness with little variance in chemical makeup, serves as an excellent example of the logic of composite materials. Essentially a geometric arrangement of stiff and flexible materials, the cell wall is tougher and

more ductile than any of its constituents, and the specifics of the geometry modulate the overall stiffness. The experiment discussed in Chapter 4, while not directly mimicking wood, explored this logic of arranging stiff and flexible material for superior properties. The report compared the mechanical response and failure mechanism of the printed sample with respect to the simulation from which it was printed. A macroscopic observation, combined with stress-strain data presented strong evidence that the sample exhibited the qualities that it was designed to exhibit, namely a measure of toughness and ductility from brittle components. Through a more thorough, microscopic, investigation, we have presented further evidence towards the quality of the experiment and the printed sample. We have shown that the strain fields observed in the simulation corresponded with delocalized damage within the sample, and present the dispersed damage as the method of fracture energy dissipation. Additionally, through higher magnification, we have shown that the damage and failure of the printed sample is not the result of any sort of interfacial failure between the two material times. The interfaces remained firm as the soft phase was strained and damaged, resulting in separation and cracks entirely within the soft phase.

Wood, not simply an historical building material, will likely continue its role in modern construction. And with better understanding of why it works will come a better efficiency of its use. One can imagine a futuristic "farm" where precision, high performance wood is grown and harvested in a sustainable cycle. This would, of course, require plenty foresight and patience (to grow according to our needs), and precise control over the growing environment (lighting, temperature, humidity, and soil nutrition). One can also imagine an alternate path: with the viability of the modeling techniques and the effectiveness of 3D printing, the road towards advanced and precisely manufactured materials and structures is being paved. Either or both of these scenarios begin here and now with these first steps. Science, however, is not directable or predictable; discovery drives innovation and vice versa, and all of it begins with the asking of "why?"

References

1. Ashby, M.F., et al., *The Mechanical Properties of Natural Materials. I. Material Property Charts*, in *Proc. R. Soc. Lond. A*1995.
2. Peterson, A.K. and B. Solberg, *Greenhouse gas emissions, life-cycle inventory and cost-efficiency of using laminated wood instead of steel construction.: Case: beams at Gardermoen airport.* Environmental Science & Policy, 2002. **5**(2): p. 169-182.
3. Glass, S.V. and S.L. Zelinka, *Moisture Relations and Physical Properties of Wood*, in *Wood Handbook - Wood as an engineering material. General Technical Report*, USDA, F. Service, and F.P. Laboratory, Editors. 2010, Forest Products Laboratory: WI.
4. Bratzel, G.H., et al., *Bioinspired noncovalently crosslinked "fuzzy" carbon nanotube bundles with superior toughness and strength.* Journal of Materials Chemistry, 2010. **20**: p. 10465-10474.
5. Sen, D. and M.J. Buehler, *Atomistically-informed mesoscale model of deformation and failure of bioninspired hierarchical silica nanocomposites.* International Journal of Applied Mechanics, 2010. **2**(4): p. 699-717.
6. Sen, D. and M.J. Buehler, *Structural hierarchies define toughness and defect-tolerance despite simple and mechanically inferior brittle building blocks.* Scientific Reports, 2011. **1**(35).
7. Dimas, L.S. and M.J. Buehler, *Influence of geometry on mechanical properties of bio-inspired silica-based hierarchical materials.* Bionspiration & Biomimetics, 2012. **7**.
8. Dimas, L.S., et al., *Tough Composites Inspired by Mineralized Natural Materials: Computation, 3D printing and Testing.* (to be published), 2013.
9. Montero, C., et al., *Relationship between wood elastic strain under bending and cellulose crystal strain.* Composites Science and Technology, 2012. **72**: p. 175-181.
10. Booker, R.E. and J. Sell, *The nanostructure of the cell wall of softwoods and its functions in a living tree.* Holz als Roh- und Werkstoff, 1998. **56**: p. 1-8.
11. Gibson, L.J., *Biomechanics of cellular solids.* Journal of Biomechanics, 2005. **38**: p. 377-399.
12. Fratzl, P. and R. Weinkamer, *Nature's hierarchical materials.* Progress in Materials Science, 2007. **52**: p. 1263-1334.
13. Speck, T. and I. Burgert, *Plant Stems: Functional Design and Mechanics.* Annual Review of Materials Research, 2011. **41**: p. 169-193.
14. Fengel, D. and G. Wegener, *Wood chemistry, ultrastructure, reactions.* De Gruyter, 1989.
15. Kerstens, S., W.F. Decraemer, and J.-P. Verbelen, *Cell walls at the plant surface behave mechanically like fiber-reinforced copmosite materials.* Plant Physiology, 2001. **127**: p. 381-385.
16. Fratzl, B., Gupta, *On the role of interface polymers for the mechanics of natural polymeric composites.* Physical Chemistry, Chemical Physics, 2004. **6**: p. 5575-5579.
17. Burgert, I., *Exploring the micromechanical design of plant cell walls.* Am J Bot, 2006. **93**(10): p. 1391-401.
18. Barnett, J.R. and V.A. Bonham, *Cellulose microfibril angle in the cell wall of wood fibres.* Biological Review, 2003. **79**: p. 461-472.
19. Cleland, R., *Cell wall extension.* Annual Review of Plant Physiology, 1971. **22**: p. 179-222.
20. Taiz, L., *Plant cell expansion: regulation of cell wall mechanical properties.* Annual Review of Plant Physiology, 1984. **35**(585-657).
21. Baskin, T.I., *Anisotropic expansion of the plant cell wall.* Annual Review of Cell and Developmental Biology, 2005. **21**: p. 203-222.
22. Jarvis, M.C., *Plant cell walls: supramolecular assembly, signalling and stress.* Structural Chemistry, 2009. **20**: p. 245-253.
23. Reiterer, A., et al., *Experimental evidence for a mechanical function of the cellulose microfibril angle in wood cell walls.* Philosophical Magazine, 1999. **79**(9): p. 2173-2184.
24. Reiterer, A., et al., *Deformation and energy absorption of wood cell walls with different nanostructure under tensile loading.* Journal of Materials Science, 2001. **36**: p. 4681-4686.

25. Altaner, C.M. and M.C. Jarvis, *Modeling polymer interactions of the 'molecular Velcro' type in wood under mechanical stress.* Journal of Theoretical Biology, 2008. **253**: p. 434-445.
26. Bergander, A. and L. Salmén, *Cell wall properties and their effects on the mechanical properties of fibers.* Journal of Materials Science, 2002. **37**: p. 151-156.
27. Fratzl, P., I. Burgert, and J. Keckes, *Mechanical model for the deformation of the wood cell wall.* Z. Metallkd, 2004. **95**(7): p. 579-584.
28. Sell, J. and T. Zimmerman, *Radial fibril agglomerations of the S2 on transverse-fracture surfaces of tracheids of tension-loaded spruce and white.* Wr Holz als Roh-und Werkst, 1993. **51**: p. 384.
29. Schwarze, F.W.M.R. and J. Engels, *Cavity formation and the exposure of peculiar structures in the secondary wall (S2) of tracheids and fibers by wood degrading basidiomycetes.* Holzforschung, 1998. **52**(2): p. 117-123.
30. Singh, A.P., *Ultrastructural features of compression wood cells in relation to bacterial decay in Pinus radiata.*, in *Recent Advances in Wood Anatomy*, D.e. al., Editor 1996, New Zealand Forest Research Institute LTD: Rotorua, New Zealand. p. 400-407.
31. Fahlén, J. and L. Salmén, *On the Lamellar Structure of the Tracheid Cell Wall.* Plant Biology, 2002. **4**: p. 339-345.
32. Kerr, A.J. and D.A.I. Goring, *The ultrastructural arrangement of the wood cell wall.* Cellulose Chemistry and Technology, 1975. **9**: p. 536-573.
33. Ruel, K., F. Barnoud, and D.A.I. Goring, *Lamellation in the S2 layer of softwood tracheids as demonstrated by scanning transmission electron microscopy.* Wood Science Technology, 1978. **12**: p. 287-291.
34. Zimmermann, T., et al., *Ultrastructural appearance of embedded and polished wood cell walls as revealed by Atomic Force Microscopy.* Journal of Structural Biology, 2006. **156**: p. 363-369.
35. Matthews, J.F., *Molecular Mechanics Simulations of Cellulose and Cellobiose*, 2008, Cornell.
36. Jarvis, M., *Cellulose stacks up.* Nature, 2003. **426**: p. 611-612.
37. Cousins, S.K. and R.M.B. Jr., *Cellulose I microfibril assembly - computational molecular mechanics energy analysis favours bonding by van der Waals forces as the initial step in crystallization.* Polymer, 1995. **36**: p. 3885-3888.
38. Wang, Y. and Y. Chen, *An atomic model of cellulose network in wood cell wall*, in *International Mechanical Engineering Congress and Exposition*2008, ASME: Boston, MA.
39. Fernandes, A.N., et al., *Nanostructure of cellulose microfibrils in spruce wood.* PNAS, 2011. **108**(47): p. E1195-E1203.
40. Wu, X., R.J. Moon, and A. Martini, *Calculation of single chain cellulose elasticity using fully atomistic modeling.* Tappi Journal, 2011. **10**(4): p. 37-42.
41. Gomes, T.C.F. and M.S. Skaf, *Cellulose-Builder: A toolkit for Building Crystalline Structures of Cellulose.* Journal of Computational Chemistry, 2012. **33**: p. 1338-1346.
42. Almond, A. and J.K. Sheehan, *Predicting the molecular shape of polysaccharides from dynamic interactions with water.* Glycobiology, 2003. **13**(4): p. 255-265.
43. Somerville, C., et al., *Toward a systems approach to understanding plant cell walls.* Science, 2004. **306**: p. 2206-2211.
44. Nishiyama, Y., *Structure and properties of the cellulose microfibril.* Journal of Wood Science, 2009. **55**: p. 241-249.
45. Pérez, S. and K. Mazeau, *Conformations, structures and morphologies of celluloses*, 2005, Centre de Recherches sur les Macromolécules, Végétales: Grenoble, France.
46. Brett, C.T., *Cellulose microfibrils in plants: biosynthesis, deposition, and integration into the cell wall.* International Review of Cytology, 2000. **199**: p. 161-199.
47. Somerville, C., *Cellulose synthesis in higher plants.* Annual Review of Cell and Developmental Biology, 2006. **22**: p. 53-78.
48. Jakob, H.F., P. Fratzl, and S.E. Tschegg, *Size and arrangement of elementary cellulose fibrils in wood cells: A small-angle X-ray scattering study of Picea Abies.* Journal of Structural Biology, 1994. **113**(1): p. 13-22.

49. Anderson, S., et al., *Studies of crystallinity of Scots pine and Norway spruce cellulose.* Trees, 2004. **18**: p. 346-353.
50. Endler, A. and S. Persson, *Cellulose Synthases and Synthesis in Arabidopsis.* Molecular Plant, 2011. **4**: p. 199-211.
51. Duchesne, I., et al., *The influence of hemicellulose on fibril aggregation of kraft pulp fibres as revealed by FE-SEM and CP/MAS C-NMR.* Cellulose, 2001. **8**: p. 103-111.
52. Donaldson, L., *Cellulose microfibril aggregates and their size variation with cell wall type.* Wood Science Technology, 2007. **41**: p. 443-460.
53. Xu, P., et al., *Dual-axis electron tomography: a new approach for investigating the spatial organization of wood cellulose microfibrils.* Wood Science Technology, 2007. **41**: p. 101-116.
54. Hanley, S.J., et al., *Atomic force microscopy and transmission electron microscopy of cellulose from Micrasterias denticulata; evidence for a chiral helical microfibril twist.* Cellulose, 1997. **4**: p. 209-220.
55. Matthews, J.F., et al., *Computer simulation studies of microcrystalline cellulose I beta.* Carbohydrate Research, 2006. **341**(1): p. 138-152.
56. Paavilainen, S., T. Róg, and I. Vattulainen, *Analysis of Twisting of Cellulose Nanofibrils in Atomistic Molecular Dynamics Simulations.* Journal of Physical Chemistry B, 2011(8): p. 3747-3755.
57. Aharoni, H., et al., *Emergence of spontaneous twist and curvature in non-euclidiean rods: Application to Erodium plant cells.* Physical Review Letters, 2012. **108**.
58. Ebringerová, A., Z. Hromádková, and T. Heinze, *Hemicellulose.* Adv Polym Sci, 2005. **186**: p. 1-67.
59. Salmén, L., *Micromechanical understanding of the cell-wall structure.* C R Biol, 2004. **327**(9-10): p. 873-80.
60. Salmén, L. and A.M. Olsson, *Interaction between hemicelluloses, lignin and cellulose: Structure-property relationships.* Journal of pulp and paper science, 1998. **24**: p. 99-103.
61. Åkerholm, M. and L. Salmén, *The oriented structure of lignin and its viscoelastic properties studied by static and dynamic FT-IR spectroscopy.* Holzforschung, 2003. **57**: p. 459-465.
62. Keckes, J., et al., *Cell-wall recovery after irreversible deformation of wood.* Nature Materials, 2003. **2**: p. 810-814.
63. Burgert, I., et al., *Tensile and compressive stresses in tracheids are induced by swelling based on geometrical constraints of the wood cell.* Planta, 2007. **226**: p. 981-987.
64. Lichtenegger, H., et al., *Variation of cellulose microfibril angles in softwoods and hardwoods - a possible strategy of mechanical optimization.* Journal of Structural Biology, 1999. **128**: p. 257-269.
65. Fratzl, P., R. Elbaum, and I. Burgert, *Cellulose fibrils direct plant organ movements.* Farady Discussion, 2008. **139**: p. 275-282.
66. Vandiver, R. and A. Goriely, *Tissue tension and axial growth of cylindrcal structures in plants and elastic tissues.* EPL, 2008. **84**.
67. Choi, H.S., et al., *Outrigger Design for High-Rise Buildings: An output of the CTBUH*2012: Council on Tall Buildings and Urban Habitat.
68. Färber, J., et al., *Cellulose microfibril angles in a spruce branch and mechanical implications.* Journal of Materials Science, 2001. **36**: p. 5087-5092.
69. Dunlop, J.W.C. and P. Fratzl, *Biological Composites.* Annual Review of Materials Research, 2010. **40**: p. 1-24.
70. *Balsa.* 2013 [cited 2013 April 22]; Available from: http://www.britannica.com/EBchecked/topic/50863/balsa.
71. Easterling, K.E., et al., *On the Mechanics of Balsa and Other Woods.* Proc. R. Soc. Lond. A, 1982. **383**: p. 31-41.
72. Atas, C. and C. Sevim, *On the impact response of sandwich composites with cores of balsa wood and PVC foam.* Composite Structures, 2010. **93**: p. 40-48.

73. Da Silva, A. and S. Kyriakides, *Compressive response and failure of balsa wood.* International Journal of Solids and Structures, 2007. **44**: p. 8685-8717.
74. Vural, M. and G. Ravichandran, *Dynamic response and energy dissipation characteristics of balsa wood: experiment and analysis.* International Journal of Solids and Structures, 2003. **40**(2003): p. 2147-2170.
75. Vural, M. and G. Ravichandran, *Experimental and Analytical Analysis of Mechanical Response and Deformation Mode Selection in Balsa Wood*, in *Major Accomplishments in Composite Materials and Sandwich Structures*, I.M. Daniel, E.E. Gdoutos, and Y.D.S. Rajapakse, Editors. 2010, Springer Netherlands. p. 717-755.
76. Yui, T., et al., *Swelling behavior of cellulose Ib crystal models by molecular dynamics.* Carbohydrate Research, 2006. **341**: p. 2521-2530.
77. Bergenstråhle, M., et al., *Cellulose crystal structure and force fields*, in *Internation Conference on Nanotechnology for the forest products industry*2010: Otaniemi, Espoo, Finland.
78. Glass, D.C., et al., *REACH Coarse-Grained Simulation of a Cellulose Fiber.* Biomacromolecules, 2012. **13**: p. 2634-2644.
79. Matthews, J.F., et al., *Comparison of Cellulose Iβ Simulations with Three Carbohydrate Force Fields.* Journal of Chemical Theory and Computation, 2012. **8**: p. 735-748.
80. Solar, M. and M.J. Buehler, *Deformation behavior and mechanical properties of amyloid protein nanowires.* Journal of the Mechanical Behavior of Biomedical Materials, 2013. **19**: p. 43-49.
81. Buehler, M.J., *Mesoscale modeling of mechanics of carbon nanotubes: Self-assembly, self-folding, and fracture.* Journal of Materials Research, 2006. **21**(11): p. 2855-2869.
82. Cranford, S.W., D. Sen, and M.J. Buehler, *Meso-origami: Folding multilayer graphene sheets.* Applied Physics Letters, 2009. **95**(123121).
83. Cabrera, R.Q., et al., *Nanomechanical and Structural Properties of Native Cellulose Under Compressive Stress.* Biomacromolecules, 2011. **12**: p. 2178-2183.
84. Peura, M., et al., *Changes in nanostructure of wood cell wall during deformation.* Materials Science Forum, 2009. **599**: p. 126-136.
85. Burgert, I., et al., *Structure-function relationships of four compression wood types: micromechanical properties at the tissue and fibre level.* Trees, 2004. **18**(4): p. 480-485.
86. Adusumalli, R.-B., et al., *Deformation and failure mechanism of secondary cell wall in Spruce late wood.* Applied Physics A, 2010. **100**: p. 446-452.
87. Keunecke, D., et al., *Micromecanical properties of common yew (Taxus baccata) and Norway spruce (Picea abies) transition wood fibers subhected to longitudinal tension.* Journal of Wood Science, 2008. **54**: p. 420-422.
88. Keten, S. and M.J. Buehler, *Asymptotic Strength Limit of Hydrogen Bond Assemblies in Proteins at Vanishing Pulling Rates.* Physical Review Letters, 2008. **100**(19).
89. Borst, K.d., T.K. Bader, and C. Wikete, *Microstructure-stiffness relationships of ten European and tropical hardwood species.* Journal of Structural Biology, 2012. **177**: p. 532-542.
90. Flores, E.I., E.A. Neto, and C. Pearce, *A large strain computational multi-scale model for the disspiative behaviour of wood cell-wall.* Computational Materials Science, 2011. **50**: p. 1202-1211.
91. Gao, H., et al., *Materials become insensitive to flaws at nanoscale: Lessons from nature.* PNAS, 2003. **100**(10): p. 5597-5600.
92. Bak, D., *Rapid prototyping or rapid production? 3D printing processes move industry towards the latter.* Assembly Automation, 2003. **24**(4).
93. Seitz, H., et al., *Three-Dimensional Printing of Porous Ceramic Scaffolds for Bone Tissue Engineering.* Wiley InterScience, 2005.
94. Roth, E.A., et al., *Inkjet printing for high-throughput cell patterning.* Biomaterials, 2004. **25**: p. 3707-3715.

95. Miller, B.W., et al., *3D printing in X-ray and gamma-ray imaging: A novel method for fabricating high-density imagine apertures.* Nuclear Instruments and Methods in Physics Research A, 2011. **659**: p. 262-268.
96. Leong, K.F., C.M. Cheah, and C.K. Chua, *Solid freeform fabrication of three-dimensional scaffolds for engineering replacement tissues and organs.* Biomaterials, 2003. **24**: p. 2363-2378.
97. *3D Printing Gallery.* [cited 2013 May 5]; Available from: http://www.jaspdesign.co.uk/3d-printing-pictures.htm.
98. Elber, G. *Escher for Real.* 2012 [cited 2013 May 5]; Available from: http://www.cs.technion.ac.il/~gershon/EscherForReal/.
99. Adhikari, R. *Fleet of FireFlies to Probe Space for Mineral-Rich Asteroids.* Tech News World, 2013.
100. Steadman, I. *Giant Nasa spider robots could 3D print lunar base using microwaves.* Wired, 2013.
101. Cranford, S.W. and M.J. Buehler, *Biomateriomics.* Springer Series in Materials Science, ed. R. Hull, et al. Vol. 165. 2012: Springer